

# AUS Repository

## Thermo-mechanical Behavior of C45 Steel over a Range of Temperatures and Loading Rates

Item Type	Thesis
Authors	Saffarini, Mohammad Hassan
Download date	2026-04-16 12:14:49
Link to Item	<a href="http://hdl.handle.net/11073/8108">http://hdl.handle.net/11073/8108</a>

THERMO-MECHANICAL BEHAVIOR OF C45 STEEL OVER A RANGE OF  
TEMPERATURES AND LOADING RATES

By

Mohammad Hassan Saffarini

A Thesis Presented to the Faculty of the  
American University of Sharjah  
College of Engineering  
in Partial Fulfillment  
of the Requirements  
for the Degree of

Master of Science in  
Civil Engineering

Sharjah, United Arab Emirates

January 2016



## Approval Signatures

We, the undersigned, approve the Master's Thesis of Mohammad Hassan Saffarini.

Thesis Title: Thermo-mechanical Behavior of C45 Steel over a Range of Temperatures and Loading Rates.

### Signature

### Date of Signature

(dd/mm/yyyy)

---

Dr. Farid H. Abed  
Associate Professor, Department of Civil Engineering  
Thesis Advisor

---

Dr. Sherif A. Yehia  
Professor, Department of Civil Engineering  
Thesis Committee Member

---

Dr. Hany A. El Kadi  
Professor, Department of Mechanical Engineering  
Thesis Committee Member

---

Dr. Aliosman Akan  
Head, Department of Civil Engineering

---

Dr. Mohamed El Tarhuni  
Associate Dean, College of Engineering

---

Dr. Leland Blank  
Dean, College of Engineering

---

Dr. Khaled Assaleh  
Interim Vice Provost for Research and Graduate Studies

## **Acknowledgment**

First of all, the ultimate thank shall be asked from Allah for watching after me as I grow in my knowledge, education, and most importantly being a good person who contributes to the best of humanity. Allah is the most compassionate, the most merciful.

I would then like to express my gratitude to my father, mother, and wife for being by my side all the way through the good and the difficult times. Also, I want to thank my family and friends for being by my side throughout my journey. It wouldn't be possible without their support and help.

Moreover, I am very thankful to my research advisor, Dr. Farid Abed for being the reason behind this success. His advice and dedication along with his advanced expertise and friendly personality made him great advisor. His understanding towards the difficulties I have been through was outstanding and for that he is an example to be followed. Additionally, Dr. Farid Abed and Dr. Akrum Abdul-Latif have conducted the experimental tests upon which this research is based, and for that I express my gratitude towards their support.

Finally, I would like to thank the members of my committee, Dr. Sherif Yehia and Dr. Hany El Kadi for their valuable suggestions.

*Dad and Mom, it wouldn't be possible without you. I hope you are Proud.*

## Abstract

This research aims to describe the behavior of C45 structural steel that is increasingly used in the oil and gas industry in environments where high temperatures and strain rates are applied. The primary goal is to introduce a systematic understanding of the thermo-mechanical ductile failure that occurs due to accumulation of micro-cracks and voids along with plastic deformation to enable proper structural design; and hence provide better serviceability. To achieve such a goal, a series of quasi-static tensile tests are conducted on C45 steel at a range of temperatures between 298 °K and 923 °K for strain rates up to  $0.15\text{s}^{-1}$ . Drop hammer dynamic tests are also performed considering different masses and heights to study the material response at higher strain rates. The stress-strain results extracted from the experimental tests are utilized to identify the material constants for the Johnson-Cook (JC) constitutive model to describe the flow stress of this type of high strength steel. Scanning electron microscopy (SEM) images are also taken to quantify the density of micro-cracks and voids of each fractured specimens which are needed to define the evolution of internal defects using an energy based damage model. The coupling effect of damage and plasticity is incorporated into the finite element (FE) software ABAQUS to develop a robust FE model that can accurately simulate different structural responses of this material. Good correlation was observed between the proposed models predictions and the experimental observations.

**Search Terms:** C45 steel; Temperature; Strain Rate; Constitutive Modeling; Damage; Finite Element; ABAQUS.

## Table of Contents

Acknowledgment .....	4
Abstract .....	6
List of Figures .....	10
List of Tables .....	13
Chapter 1 : Introduction .....	14
1.1 Problem Statement and Research Motivation .....	15
1.2 Significance of the Project .....	17
1.3 Objectives.....	18
1.4 Thesis Structure.....	18
Chapter 2 : Literature Review .....	20
2.1 High Strength Steel at High Temperatures and Loading Rates .....	20
2.2 Constitutive Modeling.....	21
2.3 Continuum Damage Mechanics .....	24
2.3.1 Definition of damage. ....	24
2.3.1.1 The atomic scale.....	25
2.3.1.2 The microscopic scale. ....	25
2.3.1.3 The mesoscopic scale.....	26
2.3.1.4 The macroscopic scale. ....	27
2.3.2 Isotropic damage.....	27
2.3.2.1 Strain equivalent hypothesis.....	29
2.3.2.2 Elastic energy equivalence hypothesis.....	30
2.3.3 Representative volume element. ....	30
2.3.4 Energy based damage model. ....	31
Chapter 3 : Research Methodology.....	33
3.1 Phase One: Literature Review.....	33
3.2 Phase Two: Experimental Program.....	33

3.2.1	Quasi-static tests. ....	34
3.2.2	Drop hammer test.....	36
3.2.3	Scanning electron microscopy. ....	37
3.2.3.1	Samples preparations.....	38
3.2.3.2	Polishing.....	38
3.2.3.3	Visual inspection of the polished samples and the modified process.....	39
3.2.3.4	EDS analysis of the chemical composition of the cracks.....	41
3.2.3.5	Final SEM observation.....	43
3.2.3.6	Images analysis – cracks density detection. ....	43
3.3	Phase Three: JC and Energy Damage Models Parameters .....	43
3.3.1	JC model parameters.....	43
3.3.1.1	Constants A, B, and n.....	44
3.3.1.2	Constant C.....	45
3.3.1.3	Constant m.....	45
3.3.2	Energy based damage model parameters. ....	46
3.4	Phase Four: Coupled Damage-Plasticity Constitutive Modeling.....	48
3.5	Phase Five: Finite Element Simulation .....	48
Chapter 4 : Experimental Tests, JC Model, and Energy Damage Model Results and Discussions.....		50
4.1	Tensile Tests.....	50
4.2	Drop Hammer Test.....	55
4.3	SEM Analysis and Damage Model Parameters .....	56
4.4	JC Model Parameters .....	59
Chapter 5 : Finite Element Simulation.....		62
5.1	Simple One-Element Axisymmetric Test .....	62
5.1.1	Effect of damage. ....	66
5.2	Quasi-Static Test Simulation.....	67

5.3	Drop Hammer Test Simulation .....	70
Chapter 6 : Conclusion and Remarks.....		76
6.1	Summary and Conclusions.....	76
6.2	Limitations and Future Research.....	77
References.....		78
Vita.....		87

## List of Figures

Figure 1: The total losses of ranger i in 1979 and alexander Kielland in 1981 were initiated by fatigue failure [1].	16
Figure 2: Scales of damage observation [77].	25
Figure 3: Separation of atomic bonds and the mechanisms of microscopic damage [77].	26
Figure 4: Section S of a certain body [79].	27
Figure 5: Damaged and effective undamaged configurations [75].	28
Figure 6: Universal Testing Machine (UTM) – a) Normal UTM [80] and b) UTM with heat chamber [81]	34
Figure 7: Geometry of the tensile test specimens at room temperature.	35
Figure 8: Geometry of the tensile test specimens at high temperatures	35
Figure 9: Drop hammer machine, a) Machine [82] and b) How the machine works [83]	36
Figure 10: Geometry of the drop hammer test specimens	37
Figure 11: Scanning electron microscope – a) SEM machine and b) Typical configuration of how the machine works [84]	37
Figure 12: Oxide spots created by the water used to clean the surface	40
Figure 13: Examples of the effects of MnS particles on the fractured surface.	41
Figure 14: EDS analysis of the surface, a) SEM image and b) EDS layered image	42
Figure 15: The percent weight composition	42
Figure 16: Illustration of the model concept [10]	47
Figure 17: Simple axisymmetric element subjected to tensile loading rate.	49
Figure 18: True stress-true strain curves at room temperature for different strain rates	50
Figure 19: True stress-true strain curves at high temperatures for strain rate of $0.0015\text{s}^{-1}$	51
Figure 20: True stress-true strain curves at high temperatures for strain rate of $0.15\text{s}^{-1}$	52
Figure 21: Stress variations against temperature for strain rate $0.0015\text{s}^{-1}$ at various strain levels.	54
Figure 22: Stress variation against temperatures for strain rate $0.15\text{s}^{-1}$ at various strain levels.	54

Figure 23: True stress-true strain curves for drop hammer test at strain rates of $390\text{s}^{-1}$ and $550\text{s}^{-1}$ .....	55
Figure 24: SEM images of fractured damaged surfaces at different temperatures for strain rate of $0.15\text{s}^{-1}$ , a) $T = 298\text{ }^{\circ}\text{K}$ , b) $T = 523\text{ }^{\circ}\text{K}$ , c) $T = 723\text{ }^{\circ}\text{K}$ , and d) $T = 923\text{ }^{\circ}\text{K}$ .....	56
Figure 25: Damage $\Phi$ at fracture for each rate of deformation at all temperatures .....	57
Figure 26: Damage $\Phi$ evolution in the material for different strain rates and temperatures .....	58
Figure 27: Temperature vs stress at different strain levels for strain rate of $0.0015\text{s}^{-1}$ .....	60
Figure 28: Temperature vs stress at different strain levels for strain rate of $0.15\text{s}^{-1}$ .....	61
Figure 29: Strain rate vs stress at different strain levels for temperature of $298\text{ }^{\circ}\text{K}$ .....	61
Figure 30: Simple axisymmetric problem description: a) Cylindrical specimen subjected to loading. b) Quarter of the cylindrical specimen with boundary conditions .....	63
Figure 31: ABAQUS model of the one-element before and after deformation a loading scenario of strain rate = $0.0015\text{s}^{-1}$ and $T = 298\text{ }^{\circ}\text{K}$ .....	64
Figure 32: Stress-strain curves at $T = 298\text{ }^{\circ}\text{K}$ for strain rates of a) $0.0015\text{s}^{-1}$ , b) $0.015\text{s}^{-1}$ , and c) $0.15\text{s}^{-1}$ .....	64
Figure 33: Stress-strain curves for strain rate $0.0015\text{s}^{-1}$ at a) $T = 523\text{ }^{\circ}\text{K}$ , b) $T = 723\text{ }^{\circ}\text{K}$ , and c) $T = 923\text{ }^{\circ}\text{K}$ .....	65
Figure 34: Stress-strain curves for strain rate $0.15\text{s}^{-1}$ at a) $T = 523\text{ }^{\circ}\text{K}$ , b) $T = 723\text{ }^{\circ}\text{K}$ , and c) $T = 923\text{ }^{\circ}\text{K}$ .....	65
Figure 35: Comparison between experimental results, JC model, and coupled plasticity-damage JC model for a) Strain rate = $0.0015\text{s}^{-1}$ at $T = 298\text{ }^{\circ}\text{K}$ , b) Strain rate = $0.15\text{s}^{-1}$ at $T = 298\text{ }^{\circ}\text{K}$ , c) Strain rate = $0.0015\text{s}^{-1}$ at $T = 923\text{ }^{\circ}\text{K}$ , d) Strain rate = $0.15\text{s}^{-1}$ at $T = 923\text{ }^{\circ}\text{K}$ .....	66
Figure 36: Mesh density of plain stress elements used in the FE simulation .....	68
Figure 37: Sample deformation process for strain rate $0.0015\text{s}^{-1}$ at room temperature, a) Un-deformed specimen, b) Deformed specimen, and c) Overlapping of deformed and un-deformed plot. ....	69

Figure 38: Force-Disp. curves at T = 298 °K for a) V = 2.5 mm/min, b) V = 25 mm/min, and c) V = 250 mm/min .....	70
Figure 39: Mesh configuration for the specimen used in the drop hammer test.....	71
Figure 40: Mesh configuration for hammer mass used in the drop hammer test .....	72
Figure 41: Mesh configuration for the rigid base used in the drop hammer test.....	72
Figure 42: Deformation process for strain rate 550 s <sup>-1</sup> .....	73
Figure 43: Comparison between the experiment deformed specimen and the FE simulation deformed specimen, a) Experiment deformed specimen and b) FE simulation deformed specimen overlapping with the un-deformed specimen .....	74
Figure 44: Contact forces-displacement curves for strain rates a) 390s <sup>-1</sup> and b) 550s <sup>-1</sup> .....	75

## List of Tables

Table 1: The number of accidents per 1000 platform-years adapted after WOAD (1996) [1]. .....	17
Table 2 Chemical composition of specimen from supplier .....	34
Table 3: Geometry of test specimen and experiments conditions for quasi-static tests .....	35
Table 4: Geometry of test specimen and experiments conditions for drop hammer test .....	36
Table 5: Polishing protocol using the grinder polishing machine .....	39
Table 6: SEM analysis results.....	57
Table 7: JC parameters implemented into the finite element simulation.....	62
Table 8: Mesh size for drop hammer test simulation.....	71
Table 9: Final Dimensions of Specimens, Experiment and Model .....	74

## Chapter 1 : Introduction

Oil and gas industry is one of the most important industries that existing life depends on to generate the energy needed for all sorts of activities. It is almost the only source of energy in many countries these days. Around 20% of the oil and gas explored around the world exist below the seabed [1]. In order to extract the oil and gas found there, engineers working in the field need to use certain kind of tools, machines, equipment, structures, materials, and even management and safety systems. The environment in that part of our earth is dangerous and not human friendly. The sizes of everything are exaggerated which reach sometimes unbelievable levels and standards. Most of the time, the dangerous nature of the environment leads engineers to use a factor of safety up to 7 due to the uncertainties faced. Materials such as high strength steel are typically used for fabricating all kinds of tooling in the industry. They are used to build ships, structures, heavy lifting machinery, subsea structures and pipelines, and even the temporary structures that are used as aids for one time job. Therefore, it is significant for the engineers who work in this industry to build stiff, durable, and light weight structures which withstand the danger accompanied with the different kinds of failures that might happen. Offshore structures are exposed to different sources of loadings that cause crack evolution within the micro-structure of the materials. Such loadings can typically be caused due to the different sources which exist within the environment in which these structures or machines operate. Fires, earthquakes, high wind speeds, hydrodynamic loads, humidity, marine growth, and coastal considerations are examples of what these structures may face when operating offshore. Hydrodynamic interaction effects, environmental loads (waves, wind, and lift loads), diffraction wave forces, effect of compliancy (relative motion), inertia force, and drag forces are major sources of providing loads that apply high strain rates due to collisions between the material and the environment elements surrounding it [2]. Moreover, accidents which cause fires and explosions are main sources of high temperatures that can be evolved within the structure's elements.

In order to account for that and to provide offshore structures with the needed "serviceability requirement," the design of these structures need to be comprehensive and efficient in terms of understanding and studying the behavior and the response of the materials that these structures are built with. All of this will eventually lead to

minimize the negative consequences such as “fatalities” and “environmental damages” of any typical failure modes by preventing brittle and “progressive structural failures” [1]. This is important in order for the structure to withstand these forces, so it becomes possible to provide enough time for evacuation and rescue.

In brief, as mentioned previously, understanding the behavior of the material in use and knowing how this material reacts after proper assessment of the exposures and loads acting on the material constitute the main work in the design phase of any project. This concept is the reason behind this research where the main goal is to study the behavior of certain type of structural steel when exposed to certain exposures in order to help the future designs to be more efficient and accurate. And for that to happen, the critical parameters which affect the behavior need to be identified. This approach will also lead to have cost effective designs without overestimating the sizes and the protection precautions.

Therefore, the significance of proposing this research, which studies the behavior of structural steel plates and the effect of damage on its response when exposed to high temperatures and intermediate strain rates, lies in understanding the capabilities of this steel when a disaster happens in order to design the structures in efficient, cost effective, and safe way.

## **1.1 Problem Statement and Research Motivation**

When the structural steel undergoes high strain rates or is exposed to high temperatures, it becomes vulnerable to experience crack initiation on the micro-structural level. In further stages, steel starts to experience internal damage where the cracks start to grow and form voids within the composition of the material. Afterwards, the material will fail at a certain point causing the failure of the structure or surrounding structural elements. Such a typical case is widely common to be faced in offshore structures due to the different sources causing high strain rates and temperatures as previously discussed. Engineers intend to understand this development within the micro-structure of the materials in order to design ductile structures and to take the necessary precautions in case failure is most probably to occur. Typical global failure in the structural integrity of the materials is experienced in many accidents before. These global failure modes caused by the development of

cracks in the material need to be understood properly and evaluated in order to avoid further accidents and events. This understanding needs to be interpreted and incorporated in the design codes as an important step towards facing the unforeseen events which may happen offshore where the environment is not human friendly and consequences might be fatal in most of the cases.

The reasons behind these failures could be due to the loads caused by ship impacts and fires due to explosions or gas release. Also, “degradation” in the structural strength due to cracks’ growth caused by fatigue or loading rates is a reason of accidents in offshore structures resulted from the failure of the inspection and maintenance system carried over there. This is leading to “catastrophic” events and accidents when they occurred at a certain point of time. Figure 1 shows a failure in “statically determinate platforms” due to crack growth in the structural elements [1]. Table 1 shows the number of accidents per 1000 platform-years adapted after Worldwide Offshore Accidents Databank (WOAD 1996). The focus in this research will be the accidents that occur due to collisions, fires, and structural damage.

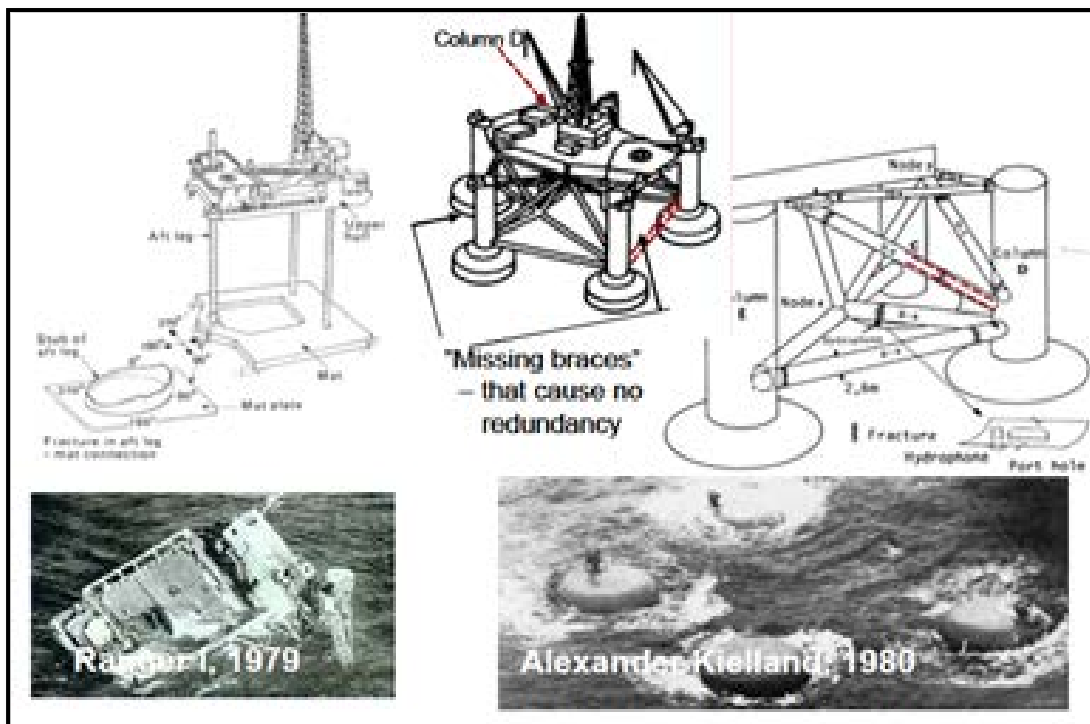


**Figure 1: The total losses of ranger i in 1979 and alexander Kielland in 1981 were initiated by fatigue failure [1].**

**Table 1: The number of accidents per 1000 platform-years adapted after WOAD (1996) [1].**

Type of accident	World wide		Gulf of Mexico	North Sea
	Mobile	Fixed	Fixed	Fixed
	1970-79 /80-95	1970-79 /80-95	1970-79 /80-95	1970-79 /80-95
Blowout	18.8/ 11.4	2.5/0.9	2.2/1.0	2.6/1.6
Capsizing/ foundering	24.0/ 19.5	0.5/0.8	0.3/1.1	2.6/0.5
Collision / contact	24.6/ 14.6	1.6/1.0	1.3/0.7	5.1/6.3
Dropped object	4.2/ 6.1	0.5/0.8	0.1/0.4	10.3/10.6
Explosion	7.4/3.3	0.7/1.6	0.3/0.4	2.6/8.3
Fire	12.3/ 11.9	2.0/7.5	1.0/7.8	18.0/42.5
Grounding	6.1/3.3	-	-	-
Spill/release	4.9/5.9	1.8/8.7	1.0/5.8	23.1/98.3
Structural damage	25.6/ 18.4	0.5/0.6	0.4/0.5	10.3/6.0

Considering the previous discussion, this research is a contribution to the state of the art in studying the behavior of C45 high strength steel that is widely used in offshore construction as structural elements, bolts, studs, gears, axles, shafts, machine parts, pins, rolls, spindles, ratchets, crankshafts, torsion bars, rams, sockets, worms, light gears, connecting rods, guide rods, and hydraulic clamps. All these applications are either used in the structure itself or as tools to build these structures. However, our concern is the structural steel and therefore its corresponding applications.

## 1.2 Significance of the Project

From previous discussions, it can be concluded that the study of the material behavior which undergoes different types of loadings and exposures is important and is needed for design purposes. It is also important to know how far the material goes when exposed to harsh conditions. This research aims to study material behavior that is widely used in certain industries when exposed to complex loadings to improve the performance of the structures built with this material, the efficiency and safety of the design, and to know the limitations of this material. Moreover, this research forms a seed in the contribution process towards implementing new considerations in the codes leading to enhance the serviceability and the general knowledge.

In specific, this research is intended to develop a comprehensive understanding of the thermo-mechanical response of C45 structural steel plates over a

range of temperatures and loading rates. It also aims at assessing the damage behavior of the material by observing the experimental results which will help to integrate an energy based damage equation that describes the internal damage evolution in C45 steel into an existing plasticity model. This coupled damage-plasticity constitutive model will be one more step towards the comprehensive understanding of the C45 steel behavior prior to its use.

### **1.3 Objectives**

The main objective of this thesis is to study the thermomechanical behavior and damage response of C45 high strength steel when exposed to high temperatures and intermediate strain rates. The detailed objectives are:

- Investigating the thermo-mechanical behavior of C45 steel plates by conducting experimental tests at different combinations of temperatures and strain rates. A series of tensile tests at a range of temperatures between 25 °C and 650 °C and strain rates up to  $10^2 \text{ s}^{-1}$  will be conducted.
- Applying the principles of continuum damage mechanics in order to evaluate and measure the damage response of C45 structural steel plates at different loading conditions.
- Utilizing the experimental results in identifying the C45 parameters for existing constitutive model; JC model.
- Utilizing the experimental results in identifying the C45 parameters for existing energy based damage model.
- Developing a finite element model that simulates different loading scenarios on C45 structural steel.

### **1.4 Thesis Structure**

The thesis starts with an introduction on the topic along with the research motivation and significance of the project. The second chapter provides a collective study on the research topics in the literature. The chapter briefly looks at the work available with brief explanations on the similar work done for high strength steel and C45 steel in specific. Then the review looks into the available constitutive models, the continuum damage mechanics principles and the energy based damage model adopted

in this study. Chapter 3 explains in details the research methodology adopted in this study describing the approach followed for each stage throughout the research. Chapter 4 is concerned with presenting and discussing the results obtained from the experimental work, the application of the constitutive model chosen for this study and the energy based damage model. In Chapter 5, finite element simulations of different loading scenarios are presented along with the verification of the constitutive model results. Finally, Chapter 6 concludes the thesis by providing a brief summary of the outcomes of this research along with the recommendations towards handling the work presented.

## Chapter 2 : Literature Review

### 2.1 High Strength Steel at High Temperatures and Loading Rates

Many research studies and experiments have been carried out in the past few decades to study the material behavior at elevated temperatures and strain rates. Steel, in particular, is one of the materials that have been extensively studied for that purpose. Researchers have been trying to understand and quantify the parameters which describe the thermo-mechanical behavior of steel. This research is among many to consider certain type of high strength steel in order to study the behavior under elevated temperatures and high strain rates.

Examples related to that field of studies in which different types of high strength steels were used are [3-38]. These studies and researches investigated the behavior of different types of high strength steel at elevated temperatures and strain rates from all perspectives. Some were investigating the shear response, while others were trying to understand the tensile and compressive stress-strain relationships. In addition, many trials on understanding the effect on the young's modulus were carried out.

Moreover, many researchers have used high strength steel as base material for experimental work to provide enough data to develop constitutive equations. These constitutive equations were mainly established to describe the flow stress behavior in the materials at elevated temperatures and strain rates [39-46].

On the other hand, and according to steel manufacturers and suppliers, offshore structures are mostly built with steel. If not the structure, other important elements of the structure or the machines used to build these structures are made of steel. Thus, it is important to understand the behavior of steel when exposed to different loading conditions. In this research, the interest is to study the behavior of C45 steel when exposed to elevated temperatures and strain rates.

Steel suppliers are providing C45 mainly to build tools, machines, or structures that sustain impact loading, sharp cutting edges, corrosion, brittle fracture, and to provide high performance and weldability [47, 48].

Triton Alloys [48], one of the major suppliers in the region, stated that "...C45 is well known for its wear resistance and other moderate properties such as thermal expansion and thermal conductivity." Also, they say that "...Grade C45, TISCRAL is widely known for its quenching and tempering ability. This kind of steel is widely used in various industries for general engineering purposes. This range is designed to withstand tremendous amount of weights and pressure. This steel plate is rust proof in their make...." Moreover, according to Triton Alloys, C45 steel is equivalent to EN 10083, JIS G4051 S45C, DIN17200 C45, UNI7846 C45, NFA AF65-C45, UNE36011 C45K, AND AISI 1042/1045.

Apart from the mentioned advantages, applications, and C45 importance, many researchers have tried to carry out experiments, studies, and analysis on C45 high strength steel. Examples of research carried out to study different perspectives of C45 in the past decades are [49-66]. These studies were attempting to understand the C45 steel in terms of formability, effect of different kinds of processes such as heat treatment and cooling, Nano-structural behavior under impact loading, distortion under cooling effect, behavior of the material when exposed to lubrication and corrosion protection processes, vibration effect, friction and wear properties, surface roughness, machinability, cavitation resistance, and effect of stress ratio and temperatures on the fracture of C45 steel.

However, the literature lacks research related to investigating the damage evolution in C45 steel and its plasticity constitutive modeling. This research will fill this gap by studying the stress-strain behavior of C45 steel under different combinations of temperatures and strain rates in an attempt to assess its coupled damage-plasticity response.

## **2.2 Constitutive Modeling**

Many constitutive models have been developed to describe the materials nonlinear behavior when exposed to high strain rates and temperatures. Some are empirical or semi-empirical relations, while others are physically-based sharing the same purpose of describing the change in mechanical properties of materials when they experience the accumulation of plastic deformation. They serve the purpose of producing the material true stress-true strain curves under different loading

conditions. These modeling concepts come from the fact that the mechanical response depends on the rate of deformation as well as the evolving temperature [4].

Examples of these models include the Johnson-Cook (JC) model [41], Steinberg-Cochran-Guinan-Lund (SCGL) model [42, 43], Zerilli-Armstrong (ZA) model [44], Mechanical Threshold Stress (MTS) model [6-9, 70, 71], Preston-Tonks-Wallace (PTW) model [4], Rusinek and Klepaczko (RK) model [4], and Voyiadjis-Abed (VA) Model [25, 73].

The Johnson-Cook model is an empirical relation that describes the flow stress in terms of strain, strain rate, and temperature without considering the coupling effect of strain rate and temperature. Not considering the coupling effect comes from the idea that the model experiences unrealistic small strain-rate dependence at high temperatures. Apart from that, the model is the most widely used among all other models that will be briefly described next [4, 41].

The Steinberg-Cochran-Guinan-Lund model is a semi-empirical relation that was aimed to model problems concerning high strain rates [42]. The model was later extended for low strain rate problems and body-centered cubic (bcc) materials by Steinberg and Lund [43]. The extended model is based on dislocation at low strain rates [5].

The Zerilli-Armstrong model consists of two different relations to describe the flow stress for two “classes” of metals, fcc and bcc metals. The model is intended to address the initial dislocation density and moving mechanism in the material. The model is based on the concept of thermal activation analysis to overcome the local obstacles preventing the dislocation from motion where the thermal flow stress component is captured by the yield stress in bcc metals and hardening stress in fcc metals [4, 44].

The Mechanical Threshold Stress model is based on the concept of the interaction between dislocations and obstacles [4]. The concept of building a complex model based on dislocation dynamics has been successful in modeling the plastic deformation of copper, tantalum [6], steel alloys [7, 8], and aluminum alloys [9]. The

model is capable of solving problems concerned with strain rates up to  $10^7 \text{ s}^{-1}$  [4, 70, 71].

The Preston-Tonks-Wallace model is similar to the Mechanical Threshold model except that this model is capable of solving problems related to “the plastic deformation in the overdriven shock regime” where the strain rates reach values greater than  $10^7 \text{ s}^{-1}$  and up to  $10^{11} \text{ s}^{-1}$  and the temperatures reach the melting point [4].

The Rusinek and Klepaczko model is a semi-physical model that deals with the total flow stress as a result of the combination between the internal stress and effective stress. The model assumes that the strain hardening is “sensitive” towards the strain rate and temperature. Therefore, as the model suggests, the internal stress is related to the strain hardening and the effective stress is related to the thermal activation [4].

The Voyiadjis-Abed model expresses the flow stress based on the concepts of the thermal activation analysis, dislocation interactions mechanisms, and the evolution of mobile dislocation density. The model considers three relations to describe the physical basis of microstructure, crystal structure, and atoms distribution for three material classes which are fcc, bcc, and hcp metals. The model was later modified to account for the flow stress of ferrite steel at low and high strain rates and temperatures by considering the evolution equation of the dislocation density resulted from the strain hardening [4, 25, 73].

As previously mentioned, these models share the same purpose of defining the flow stress in the material due to the effect of the strain rate and temperatures.

The JC model is chosen to be considered in this research because of its capability to simulate the flow stress within the range of temperatures and strain rates adopted in the experimental program. Also, the JC model is already implemented in the finite element software ABAQUS easing the use of the model.

## **2.3 Continuum Damage Mechanics**

As previously explained, the structural materials experience harsh loadings and exposures resulting in the loss of their physical properties and mechanical characteristics. Hence, it is important to study the stages that these materials go through in order to understand and properly assess the changes which happen on the microstructural level.

In the past half a century, great attention was drawn to the study of the microstructural level of the material in order to understand and “improve” the material in all aspects [75]. This has led to the enhancement of the serviceability and the performance of the materials in different types of industries. This part of studying the mechanics of materials is concerned with the study of the damage that occurs on the microstructural level which causes “a significant influence on the safety aspect of engineering structures.” It has been an interest to the designers, in specific, due to its great role in determining the “useful life” of the material and more importantly its role in predicting the failure mechanism and at which stage [75]. This is an important consideration for many designers in engineering application leading them to properly assess the lifetime of the materials they use and ultimately improve the performance of their designs. In order to express the previous in better words, Krajcinovic [76] stated that “...the question is not whether the damage is present in a structure such as an aircraft, car or steel bridge, but instead whether the structure is in its real, damaged state fit for the intended purpose. The question also whether the structure is reliable and how much longer will it last or function as intended.”

### **2.3.1 Definition of damage.**

According to Murakami [77], damage is defined as the “development of cavities in the microscopic, the mesoscopic, and the macroscopic processes of fracture in materials together with the resulting deterioration in their mechanical properties.” In more explicit words, it all starts with a breakage in the atomic bond or a defect in the atomic array leading to the nucleation of micro-cavities. These micro-cavities start to grow and form coalescence between each other on a mesoscopic level leading to the formation of macro-cracks. Final stage would be the growth of these macro-

cracks resulting into the fracture of the material. Figure 2 shows the fracture process starting from the atomic scale towards the formation of the macro-cracks.

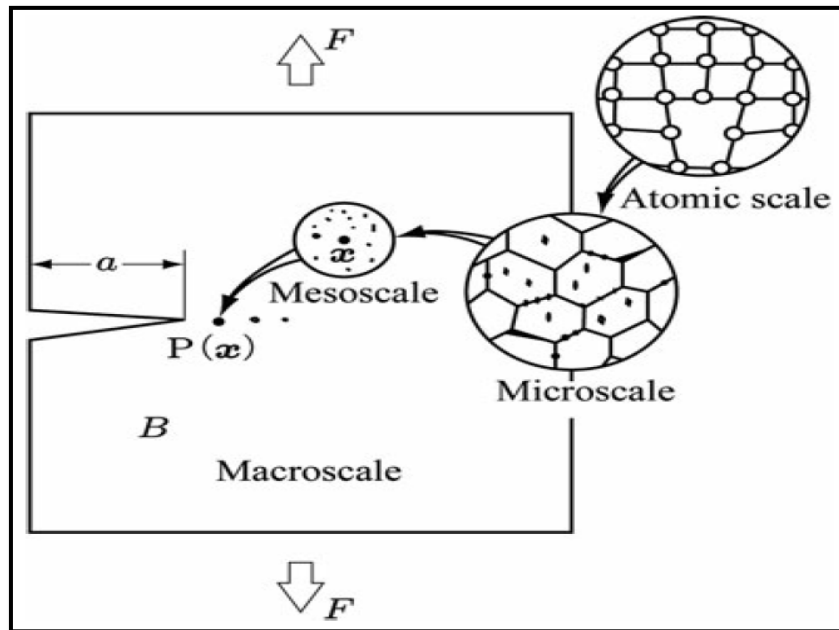


Figure 2: Scales of damage observation [77].

In general, these four scales, where the damage observations exist, can be explained in the following manner [77, 78]:

### 2.3.1.1 The atomic scale.

The material physical and mechanical properties are shaped by the behavior of the molecules forming the material, their array, and the interaction bonding and forces between these molecules. The damage at that scale starts when a disturbance to the bonds or to the array formed in between the molecules exists [77].

### 2.3.1.2 The microscopic scale.

At this level, there exists continuity in the material where the visual field has a “discontinuous structure as a whole.” In there, the damage can be observed in the micro-cavities, micro-cracks, or de-cohesion in the microstructure of the material [77]. The microscopic mechanism of material damage consists of four mechanisms which are cleavage, growth and coalescence of micro-voids, glide plane de-cohesion and void growth that occurs due to grain-boundary diffusion. Damage starts with a

tensile de-cohesion in crystal planes intrinsic to the crystals without any plastic deformation accompanied followed by a fracture of the inclusion due to accumulation of the plastic deformation coming from the stress concentration induced by pile-up of dislocation to inclusions making it the second stage. The increase in the plastic deformation results in the nucleation of new surfaces on specific slip planes leading to the fracture of crystalline material where the cross sectional of the material reduces almost to zero. Finally, when the material is exposed to a temperature higher than  $1/3$  of the absolute melting temperature, a diffusion of vacancies gives rise to cavities on grain boundaries perpendicular to the tensile stress resulting in the microscopic de-cohesion or fracture [77]. These four steps are shown in Figure 3.

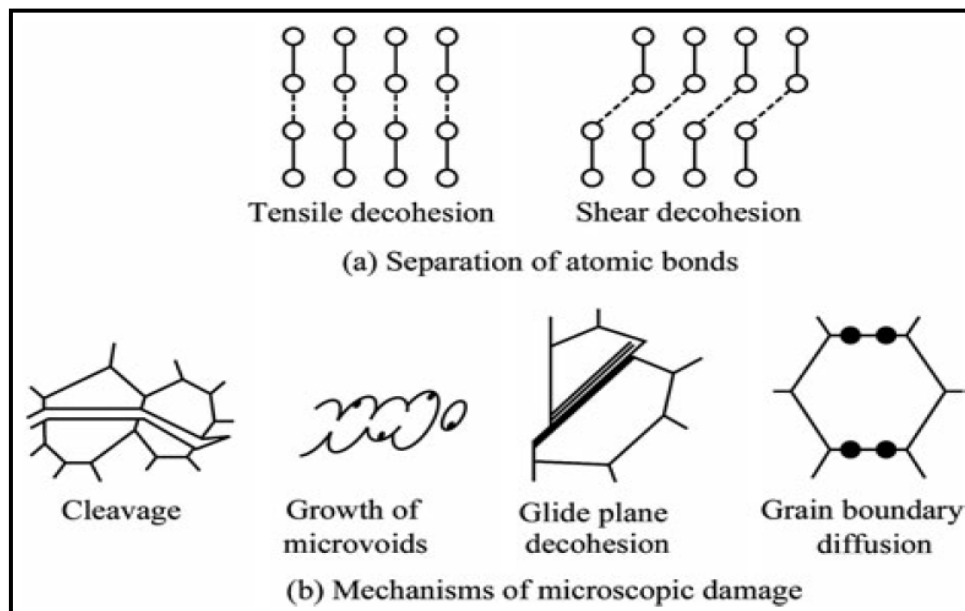


**Figure 3: Separation of atomic bonds and the mechanisms of microscopic damage [77].**

At this scale, the mechanisms of strain and damage can easily be understood and the hypotheses are taken to write constitutive equations at the macro-scale [78].

### **2.3.1.3 The mesoscopic scale.**

On a larger scale than the microscopic level, there is a discontinuity between the microstructures represented by the micro-cracks. If a region around a random point is considered at an appropriate scale, where the mechanical state value is averaged over that region so it can be expressed as a continuous function, this scale then is called a mesoscale and the material is to be idealized as a continuum [77].

#### 2.3.1.4 The macroscopic scale.

It is the scale where every point in the material can be considered as a part of a continuum. Hence, the material consists of many material points where the density and the relevant physical quantities can be defined in the material [77].

#### 2.3.2 Isotropic damage.

According to Kachanov [79], isotropic damage is a condition in which the cracks and voids are equally distributed in all directions. In order to understand the mathematical representation of the isotropic damage, let us consider a section “S” of a body with a unit normal  $\nu$  as shown in Figure 4.

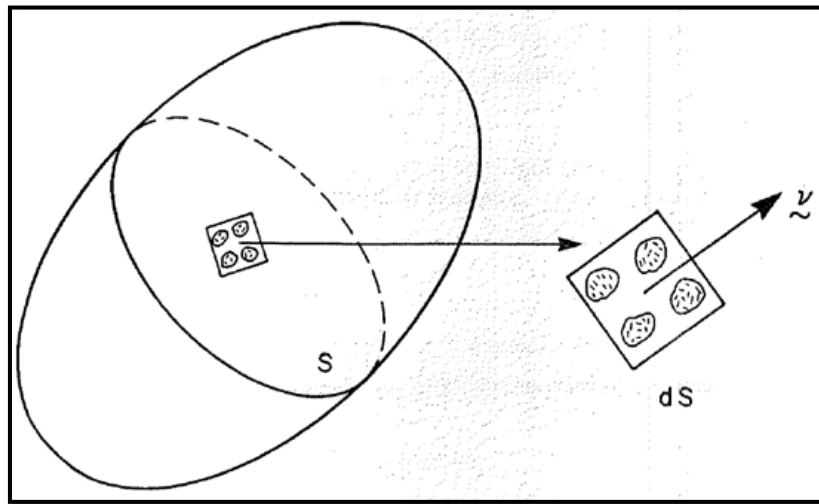
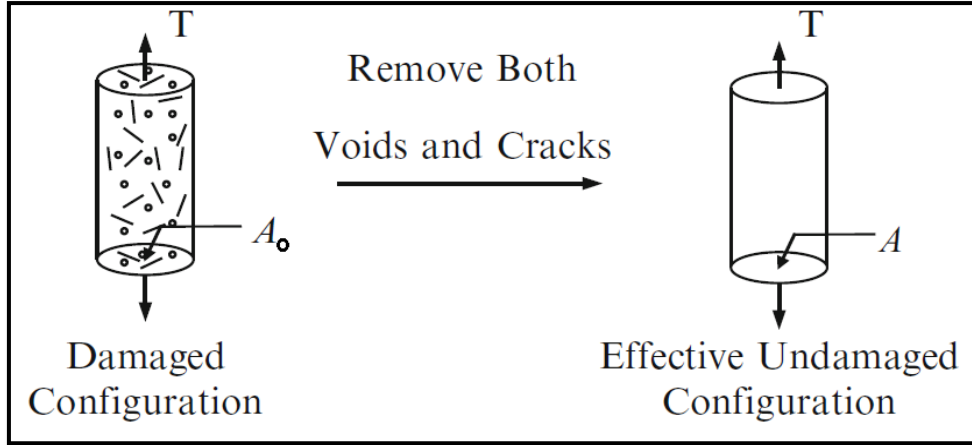


Figure 4: Section S of a certain body [79].

If  $A_0$  is assumed to be the initial area of the undamaged section,  $A$  is to be assumed the area that will be lost after the damage occurs at certain part of the section “S”. Therefore, the value  $A_0 - A$  will be the actual area of the section after the occurrence of the damage.

In Figure 5, let us consider one body in the state of damage and a “fictitious” body if we can remove the voids and cracks caused by the damage occurred.



**Figure 5: Damaged and effective undamaged configurations [75].**

Therefore, in defining a damage variable  $\phi$ , its value must be zero in the fictitious body. The isotropic damage variable  $\phi$  is thus defined as:

$$\phi = \frac{A_0 - A}{A_0} \quad (1)$$

where  $A_0$  is the cross-sectional area in the damaged body and  $A$  is the cross-sectional area in the fictitious body with  $A_0 > A$ . It is clear that when a body is undamaged, i.e.,  $A_0 = A$ , then  $\phi = 0$ .

The stress in the fictitious body is called the effective stress and is denoted by  $\bar{\sigma}$  where the stress in damaged body is denoted by  $\sigma$ . The value of the effective stress  $\bar{\sigma}$  is obtained using the relation  $\bar{\sigma} A = \sigma A_0$ . Therefore, the below equation can be obtained:

$$\bar{\sigma} = \frac{\sigma}{1 - \phi} \quad (2)$$

According to Voyiadjis [75], the equilibrium condition between the effective stress and normal stress is appropriate only in the dilute damage regime.

In the case of isotropic damage, the damage variable is scalar since the cracks and voids are distributed equally in all directions. Two major scalar damage variables are widely used; the first scalar damage variable is defined in terms of the reduction in cross sectional area as previously described while the second scalar damage variable

is defined in terms of the reduction in the elastic modulus. The second variable is computed based on one of the following two hypotheses:

- Hypothesis of elastic strain equivalence in which the strain in the damaged body  $\varepsilon$  is assumed to be equal to the effective strain  $\bar{\varepsilon}$  in the fictitious body.
- Hypothesis of elastic energy equivalence in which the elastic strain energy is assumed to be equal in both configurations.

### ***2.3.2.1 Strain equivalent hypothesis.***

Using the elastic strain equivalence hypothesis, we assume that the effective strain is equal to the actual strain in the damaged body:

$$\bar{\varepsilon} = \varepsilon \quad (3)$$

Applying equation (3) to both configurations, the damaged and the undamaged bodies, the following is obtained:

$$\sigma = E \varepsilon \quad (4)$$

$$\bar{\sigma} = \bar{E} \bar{\varepsilon} \quad (5)$$

Substituting for  $\sigma$  and  $\varepsilon$  using equation (3) and equation (4) into equation (5) will result in the relation between the effective modulus of elasticity, the modulus of elasticity of the damage body, and the damage variable as represented by equation (6):

$$\bar{E} = \frac{E}{1 - \phi} \quad (6)$$

Rearranging equation (6) in order to obtain the damage variable in terms of the modulus of elasticity in both configurations will give equation (7):

$$\phi = 1 - \frac{E}{\bar{E}} \quad (7)$$

This damage variable may be rewritten in the form represented by equation (8) to express the value of modulus of elasticity in the damaged body.

$$E = \bar{E} (1 + \phi) \quad (8)$$

### 2.3.2.2 Elastic energy equivalence hypothesis.

Using the hypothesis of elastic energy equivalence, one assumes the complementary elastic strain energy  $\frac{\sigma^2}{2E}$  to be equal in both configurations.

$$\frac{\sigma^2}{2E} = \frac{\bar{\sigma}^2}{2\bar{E}} \quad (9)$$

Substituting for  $\sigma$  from equation (2) into the above equation and simplifying it:

$$\bar{E} = \frac{E}{(1-\phi)^2} \quad (10)$$

Rearranging equation (10) gives the following result:

$$\phi = 1 - \sqrt{\frac{E}{\bar{E}}} \quad (11)$$

Despite that both hypotheses are used by researchers, it is believed that the second hypothesis is more valid since it involves energy formulation [75].

The second scalar damage variable  $\phi$  may be defined as follows:

$$\phi = \frac{\bar{E}-E}{E} \quad (12)$$

Where  $E$  is the elastic modulus in the damaged state and  $\bar{E}$  is the effective elastic modulus in the fictitious state with  $\bar{E} > E$ .

### 2.3.3 Representative volume element.

In order to understand the damage at the microscopic level by the principles of continuum mechanics, it is a “must” to represent the mechanical effects of the microstructure as a macroscopic continuous field in the material in order to homogenize these effects [77].

Therefore, let us consider Figure 2 shown earlier. If we take a small region  $\mathbf{V}$  of a mesoscale around a material point  $\mathbf{P}(\mathbf{x})$  in a body  $\mathbf{B}$ , and if the region  $\mathbf{V}$  is the smallest that satisfies the below condition,  $\mathbf{V}$  then will be considered as the

Representative Volume Element: "... the material with discontinuous structures in region  $V$  can be statistically homogeneous and the mechanical state of the material in  $V$  can be represented by the statistical average of the mechanical variables in  $V$ " [77].

According to Murakami [77], if at every point of the body  $B$  we can take an RVE, the material can be idealized as a continuum by "means of the statistical average of the mechanical state." The mechanical state of the continuum is unique only if the RVE is the statistical representation of the actual material when the following two conditions are satisfied:

- The RVE is large enough to contain a sufficient number of discontinuities.
- The size of RVE is small enough so that the variation of the macroscopic variable in it may be insignificantly small.

The size required for  $V$  to be an RVE depends on the type of the material and the type of damage. The typical sizes of RVE according to the material type are as follow [77]:

- Metal and ceramics  $(0.1 \text{ mm})^3$
- Polymer and composites  $(1 \text{ mm})^3$
- Timber  $(10 \text{ mm})^3$
- Concrete  $(100 \text{ mm})^3$

Murakami [77] has stated that since brittle and fatigue damage are much more localized than creep and ductile damage, the size of an RVE required to represent the brittle and the fatigue damage should be larger than that for the creep damage and the ductile damage.

#### **2.3.4 Energy based damage model.**

Simulating the damage evolution in steel is a concern when it comes to studying the effect of damage on the behavior of steel and its response to different exposures. However, the ordinary experimental methods are costly and time consuming, not mentioning that in some cases, they can be difficult to perform. This is because measuring the damage evolution using the ordinary methods requires many specimens in which the damage at each loading point throughout the deformation

process needs to be measured. In other words, a single specimen will be loaded to a certain strain level and then will be cut to measure the area of cracks. Afterwards, the same will be repeated with a new specimen at another strain level. Accordingly, to get proper description of the damage evolution, many specimens need to be tested at many points during the deformation process. Apart from that, the damage models that are integrated in the “commercial finite element codes” require careful handling and “great experience” to obtain realistic results [10]. Hence, the need to choose a simpler model that simulates the damage evolution in steel is significant. Therefore, a related energy based model available in the literature which is suitable for different loading conditions and metals is used and will be integrated into the suggested constitutive models for the purpose of extending the capabilities of these constitutive models.

In this research, an energy based damage model developed by Abed et al. [10] will be utilized to describe the evolution of micro-cracks and voids throughout the inelastic deformation. This model is concerned with describing the damage in steel as a function of the dissipated plastic energy and the damage at fracture. The model is based on “the hypothesis that damage dissipates nonlinearly as a function of the effective accumulated plastic strain taking into consideration the global effect of nucleation, growth, and coalescence of micro-voids in a ductile failure process” [10]. The details of the model are discussed in the next chapter.

## **Chapter 3 : Research Methodology**

The main goal of the proposed research is to describe the thermo-mechanical behavior of C45 structural steel experimentally and analytically. In order to achieve this goal, the work has been divided into the following phases:

### **3.1 Phase One: Literature Review**

This phase is concerned with carrying out an extended literature review to perform a collective survey about the experimental and theoretical studies that have been done on the material. In addition, it is planned to look-up for the constitutive models that can be implemented to further study the behavior of the material in concern. Also, the literature review is intended to study and understand the mechanics of continuum damage in order to be able to apply the concepts in the matter in hand.

### **3.2 Phase Two: Experimental Program**

The main objective of the experimental work is to characterize the mechanical properties and characteristics of C45 steel at different temperatures and strain rates. The results obtained are used to define the needed constants for the suggested constitutive model that will simulate the nonlinear behavior of the material. Afterwards, the damage variable is studied and determined through the area measurements using the Scanning Electron Microscope (SEM) to define the parameters of the energy based damage model which will be integrated in the JC constitutive model to describe the damage response of C45 steel.

It should be mentioned that the experiments were done prior to this research work where the tensile tests at room temperature along with the SEM processing were conducted by Dr. Farid Abed while the high temperatures and drop hammer tests were conducted by Dr. Akrum Abdul-Latif in his lab in Paris, France. This research analyzes all these experimental results and their outcomes.

The proposed experimental program considers three types of tests that will be used to define the behavior of C45 steel over a range of temperatures and strain rates. These tests are Quasi-Static Tests, Drop Hammer Test, and Scanning Electron Microscopy. The chemical composition of C45 steel is shown in Table 2.

**Table 2 Chemical composition of specimen from supplier**

Steel	C	Mn	Si	S	P	Cu	Iron
Mass %	0.45	0.62	0.25	0.02	0.19	0.02	98.45

### 3.2.1 Quasi-static tests.

In these tests, the samples are subjected to tension until fracture at predefined strain rates while being exposed to a range of temperatures. The following two scenarios were considered:

- Tensile tests at constant temperature and three different deformation rates of 5 mm/min, 50 mm/min, and 500 mm/min were applied. Two samples (S1 and S2) were tested per each loading rate using a Universal Testing Machine (UTM) with 100 kN capacity as shown in Figure 6.a.
- Tensile tests at three different temperatures for two different deformation rates were performed. The scenario was considering heating the samples with a heat chamber and simultaneously loading the samples at predefined deformation rate. The samples were exposed to two deformation rates of 5 mm/min and 500 mm/min at 3 different temperatures of 523 °K, 723 °K, and 923 °K. The specimens were tested using the Universal Testing Machine (UTM) with a heat chamber to apply the needed temperatures as shown in Figure 6.b.

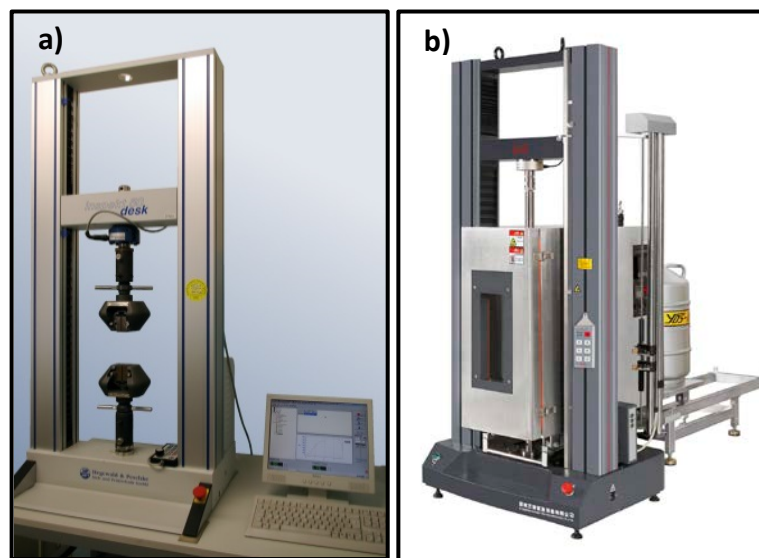


**Figure 6: Universal Testing Machine (UTM) – a) Normal UTM [80] and b) UTM with heat chamber [81]**

A summary of the specimen geometry for the previously explained test scenarios is given in Table 3 and Figures 7 and 8.

**Table 3: Geometry of test specimen and experiments conditions for quasi-static tests**

Tensile Test at Room Temperature ( $T = 298 \text{ }^\circ\text{K}$ )						
V (mm/min)	5		50		500	
Sample	S1	S2	S1	S2	S1	S2
t (mm)	4.988	9.83	9.95	10.12	9.98	10.12
w (mm)	11.77	12.85	12.12	12.23	12.25	12.23
l (mm)	54	54	56.62	57	56.62	57
Tensile Test at High Temperatures						
V (mm/min)	5			500		
T (Kelvin)	523	723	923	523	723	923
Diameter (mm)	6	6	6	6	6	6
Length (mm)	39	39	39	39	39	39

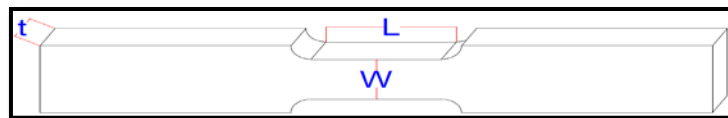


**Figure 7: Geometry of the tensile test specimens at room temperature**

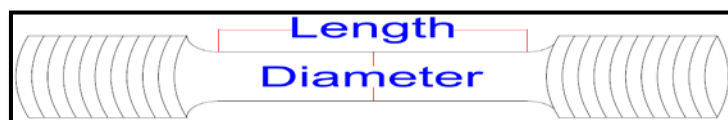


**Figure 8: Geometry of the tensile test specimens at high temperatures**

### 3.2.2 Drop hammer test.

The drop hammer test is a dynamic test used to determine the behavior of a sample at a strain rate between  $10$  and  $10^2 \text{ s}^{-1}$ . During the test, a mass falls from a given height on a sample transferring the potential energy in the mass into kinetic energy in the sample as shown in Figure 9. Only two specimens were tested as illustrated in Table 4 and Figure 10.

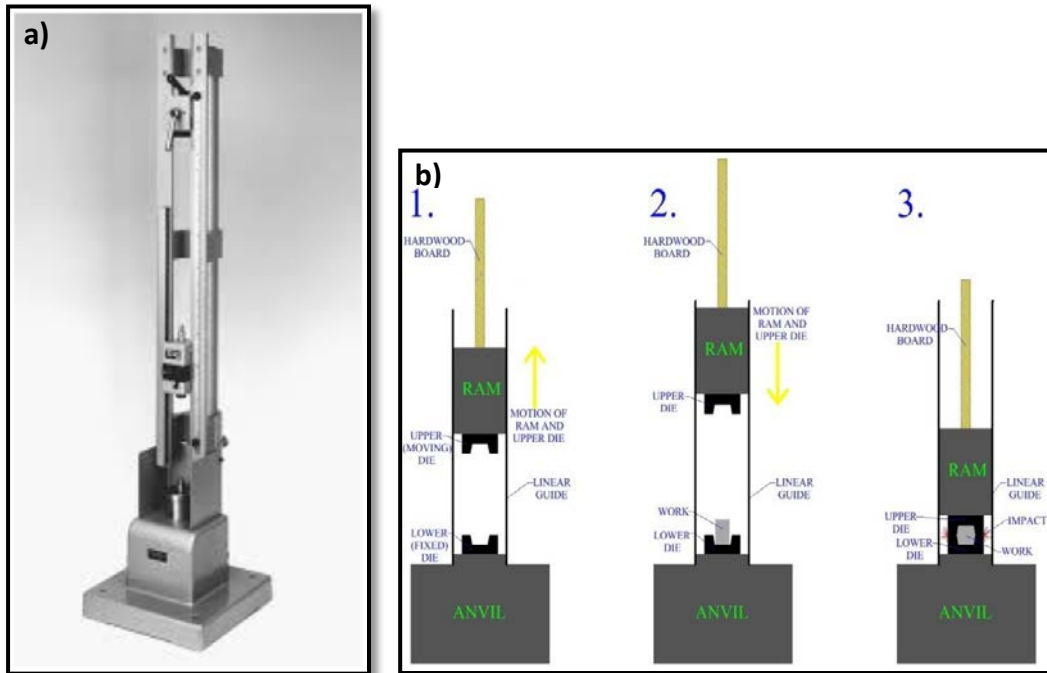


Figure 9: Drop hammer machine, a) Machine [82] and b) How the machine works [83]

Table 4: Geometry of test specimen and experiments conditions for drop hammer test

Drop Hammer Test		
Hammer Mass (Kg)	28	56
Drop Height (m)	4	2
Hammer Density ( $\text{Kg/m}^3$ )	7850	7850
Hammer Height (mm)	454	909
Sample Initial Height (mm)	16.11	16.17
Sample Initial Diameter (mm)	8.05	8

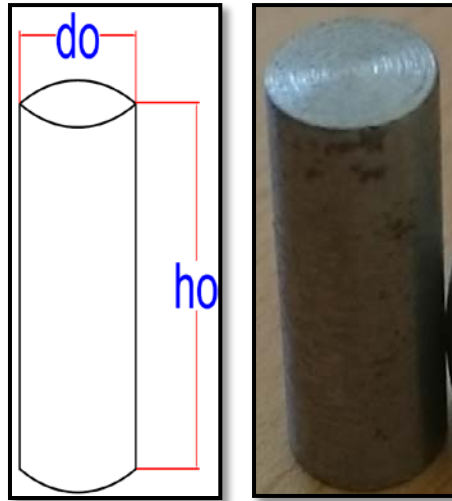


Figure 10: Geometry of the drop hammer test specimens

### 3.2.3 Scanning electron microscopy.

This part of the experimental program is intended to characterize the material damage using the Scanning Electron Microscopy equipped with an Energy Dispersive Spectrophotometer (EDS) Detector, Back Scattered Electron (BSE) Detector, and Secondary Electron (SE) Detector as shown in Figure 11.

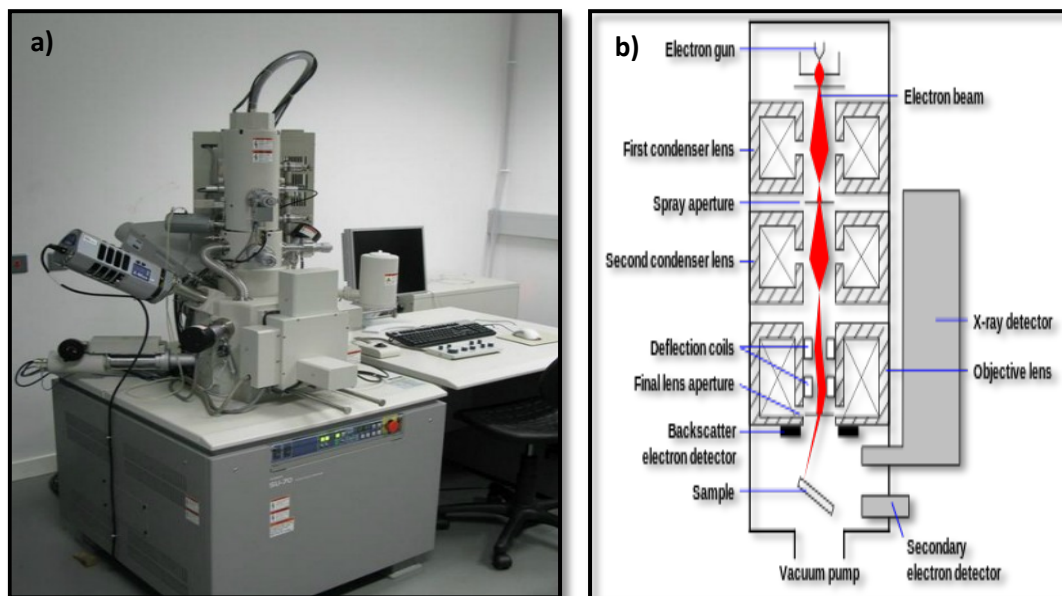


Figure 11: Scanning electron microscope – a) SEM machine and b) Typical configuration of how the machine works [84]

By using the SEM Machine, the density of micro cracks at fracture for each quasi-static test condition will be determined. Afterwards, the micrographs will be analyzed using software (ImageJ) that detects the variation of contrast between pixels.

On the SEM photograph, the cracks will appear dark because the electrons are not reflective to the sensor. The higher the contrast between cracks and the surface, the better the photograph will be. Also, the polished surface has to be flat and horizontal to get a good quality photograph.

### ***3.2.3.1 Samples preparations.***

The fractured surface of each sample after each test was polished using a grinder polish machine. A cut through the sample is needed to get clear fractured surfaces. In order to have a clear fractured surface without changing the mechanical property of the samples, erasing the cracks inside the samples, or even causing any further cracks, the following shall be noted about the process:

- The process shall not be violent in order to maintain cracks as well as their orientation and size. Milling cutting process can cause such a problem.
- Different tools shall be compared in order to properly evaluate their effects on the samples. Therefore, tools such as the manual saw, circular diamond saw, and grinding machine were tested in order to decide which tool is better to achieve the objective. It was found that the manual saw is the best available option since it does not heat the sample in a way that can change the property of the material and its cutting speed can be easily controlled.

It is worth mentioning that better results can be obtained by using an automatic precision micro-cutting machine since it is usually used in laboratories to cut metal samples before analysis at a very low feed speed of 6 mm/min. Unfortunately, this option was not available at the time of the experiment.

### ***3.2.3.2 Polishing.***

After preparing the tensile tests samples and properly cutting the test samples, the samples were polished with special grinder polishing machine in order to obtain

flat surfaces. The steps to achieve the aforementioned objective were done as the following:

- The protocol for polishing a steel sample in terms of the size of the sand, the duration, and the velocity of the disk is defined in Table 5.

**Table 5: Polishing protocol using the grinder polishing machine**

Type	PG	FG	DP1	DP2	OP
Support	Papier SiC 320	MD-Largo	MD-Dur	MD- Nap	MD-Chem
Suspension		DiaPro Allegro/Largo 9 $\mu\text{m}$	DiaPro Dur 3 $\mu\text{m}$	DiaPro Nap B 1 $\mu\text{m}$	OP-S
t/m	300	150	150	150	150
Load	30	30	15-30	10	10
Time (min)	1	5-10	5	5	1-5

- Using the grinder polishing machine, the fracture surface of each sample was polished with 4 different abrasive papers at decreasing grit size of SiC240, SiC350, SiC800 and SiC1000.
- It is recommended to use diamond powder (DiaPro) 3 $\mu\text{m}$ , however; the smallest diamond powder size available was 6 $\mu\text{m}$ . Therefore, the diamond powder with size of 6 $\mu\text{m}$  in diameter was used to get a mirror surface. This last process was intended to erase the scratches made by the abrasive papers.

### ***3.2.3.3 Visual inspection of the polished samples and the modified process.***

After polishing the surface, the samples were observed using the SEM machine in order to find out whether the process was successful or not. It was found that the results were not good enough because the diamond powder created scratches that were larger than the cracks leading to inaccurate detection of cracks using ImageJ. Also, some oxide spots created by the water used to clean the surface were discovered as shown in Figure 12.

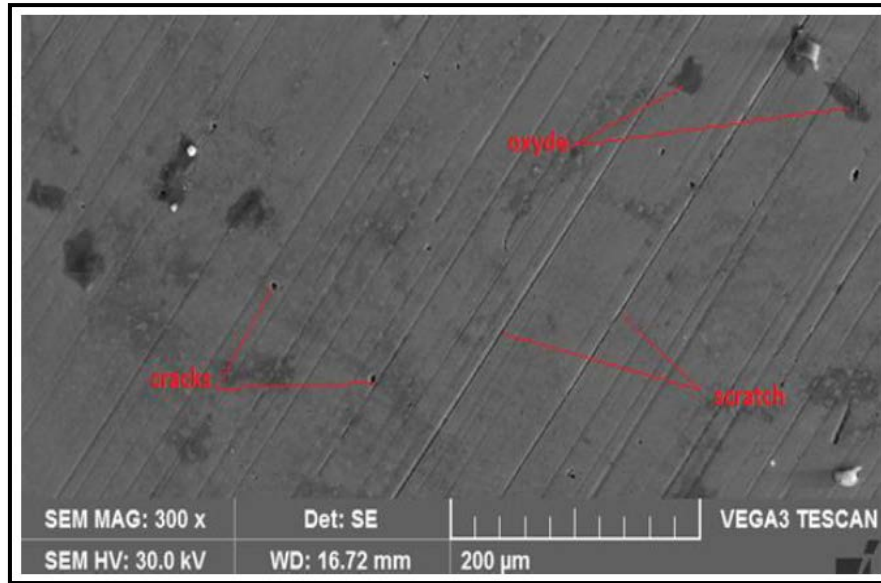


**Figure 12: Oxide spots created by the water used to clean the surface**

The following modifications have been adopted in order to obtain clear fractured surfaces to be analyzed by the software ImageJ:

- Along with using the diamond powder in the last step, the air pressure and the acetone were used in order to clean the surface. It is worth mentioning that the Dye Penetrant Inspection Method – or Liquid Penetrant Inspection Method - was initially aimed to be used as an additional modification to increase the contrast between the deep cracks and the surface. The method is based upon capillary action in which a colored fluid penetrates into voids and after adequate penetration time, the surface is cleaned to apply a second product, the developer, to draw up the penetrant in order for the deep cracks to appear in color. Although this control method is often used to detect cracks in casting, forging, and surface welding, this method cannot be combined with SEM because the liquid used will degas in the chamber of the SEM and prevent a vacuum from forming.
- At first, the Secondary Electron (SE) detector was used to observe the fractured surfaces. Despite the improved quality of the images, some dark spots that were thought to be cracks were clearly seen and some scratches caused by the previous polishing process were observed. These would cause inaccuracy in detecting the cracks by the software. Therefore, the other

detector of the SEM which is the Back-Scattered Electron (BSE) detector was used since it is more sensitive to the embossed design and chemical composition. This sensor was found to provide much better results for observing the voids in the samples by giving a significant contrast in the pixels.

#### ***3.2.3.4 EDS analysis of the chemical composition of the cracks.***

Generally, some intermetallic compounds such as MnS particles can exist on the fractured surfaces. These particles are hard to break, therefore; they leave some kind of prints or create voids after being wrested from the surface during the polishing process as shown in Figure 13. Thus and in order to avoid the possibility of confusing the cracks with prints that were left by these intermetallic compounds, a chemical composition analysis of the surface has to be performed.

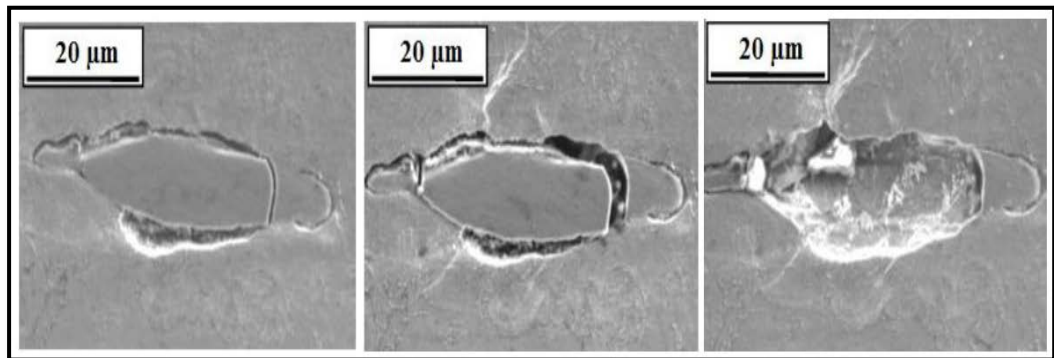


**Figure 13: Examples of the effects of MnS particles on the fractured surface**

In order to prove whether these voids were cracks or prints left from the intermetallic compounds, the EDS detector in the SEM machine is used to analyze the chemical composition of the voids by mapping the surface. Using this process, the area of the surface is scanned and each element is detected and highlighted in color as shown in the Figure 14.

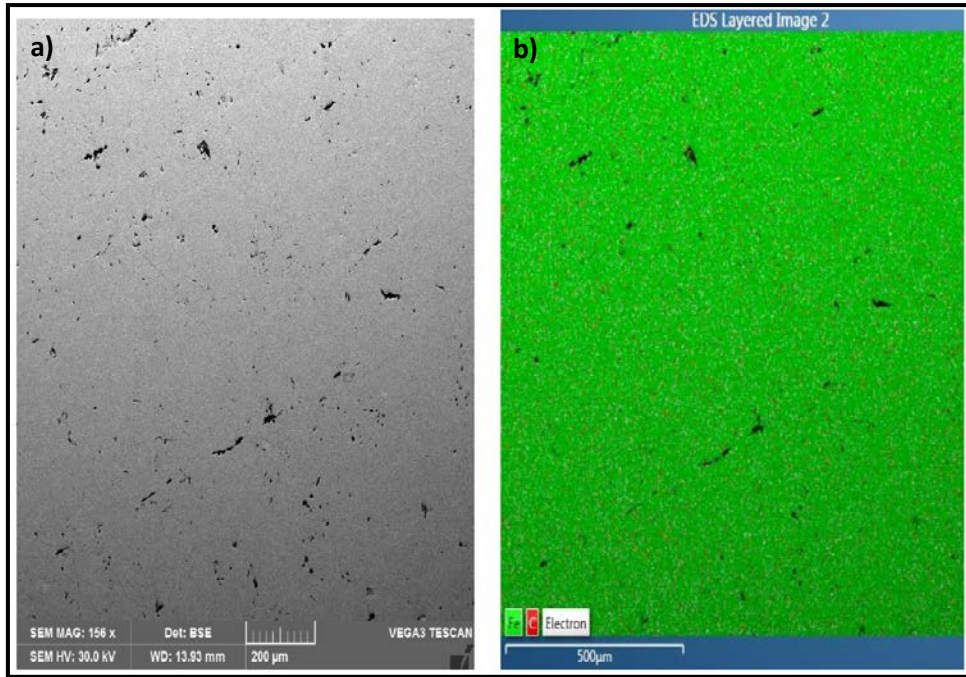


**Figure 14: EDS analysis of the surface, a) SEM image and b) EDS layered image**

In Figure 14.b, holes appear in black, iron appears in green, and carbon appears in red. These two elements are homogeneously located except in the voids where none of these elements are detected. This means that the chemical composition inside the cracks is different from the surface. Using the percent weight composition developed by the software as shown in Figure 15, some small quantities of sulfur can also be noticed in addition to iron, carbon, and manganese.

Element	Wt%	σ
Fe	93.6	0.3
C	5.1	0.2
Mn	0.6	0.0
Si	0.3	0.0
Al	0.2	0.0
Sr	0.2	0.1
Pb	0.0	0.1
P	0.0	0.0
Cr	0.0	0.0
Cu	0.0	0.0
Zn	0.0	0.0
S	0.0	0.0
Ca	0.0	0.0
Na	0.0	0.0
Mg	0.0	0.0
Ti	0.0	0.0
Ni	0.0	0.0

**Figure 15: The percent weight composition**

Particles and steel do not have the same behavior because these particles, even though very hard, can be removed from steel during the polishing process. Therefore, it can be concluded that all the cracks and particles that have been detected with ImageJ can be considered as damage and their density which will be presented in the following chapters can be used to define the damage variable.

#### ***3.2.3.5 Final SEM observation.***

After applying the aforementioned modifications, it was possible to provide good quality SEM images. Two different scales were used to produce the tensile tests images; 100  $\mu\text{m}$  (500x) and 50  $\mu\text{m}$  (1000x). In addition, images of scale 200  $\mu\text{m}$  (200x) were also produced with higher resolution in order to detect small details that are not seen with lower resolutions for validation purposes.

#### ***3.2.3.6 Images analysis – cracks density detection.***

To calculate the density of cracks, the software ImageJ was used to analyze the images by detecting the contrast between the pixels which contain cracks and the pixels that don't contain cracks. In other words, it determines the fraction of area where the contrast is the highest in which the cracks appear in dark. In order to obtain a good average crack density, 5 to 7 different areas on the sample surface between the edge and the middle were selected to be analyzed and the average was considered.

### **3.3 Phase Three: JC and Energy Damage Models Parameters**

This phase will be concerned with determining the constant parameters in JC and Energy Based Damage models using the experimental results. Afterwards, the models will be used in order to perform the finite element simulation using the software ABAQUS.

#### **3.3.1 JC model parameters.**

The Johnson Cook model was proposed by Johnson and Cook in 1983. As explained earlier, it is considered as the most widely used among other models. The model describes the material behavior as a function of temperature, strain, and strain

rate empirically without considering their coupling effects. These factors represent the material constitutive behavior and is determined as follows:

$$\sigma = [A + B(\varepsilon_p)^n] \left[ 1 + C * \ln \left( \frac{\dot{\varepsilon}}{\dot{\varepsilon}_0} \right) \right] \left[ 1 - \left( \frac{T - T_{ref}}{T_{melt} - T_{ref}} \right)^m \right] \quad (13)$$

where  $\sigma$  is the equivalent stress,  $\varepsilon_p$  is the plastic strain,  $\dot{\varepsilon}$  is the strain,  $\dot{\varepsilon}_0$  is the reference strain rate,  $T$  is the temperature of the sample,  $T_{melt}$  is the melting temperature of the material,  $T_{ref}$  is the reference temperature,  $A$  is the yield stress of the material at a reference deformation conditions,  $B$  is the strain hardening constant,  $C$  is the strain rate strengthening coefficient,  $n$  is the strain hardening constant, and  $m$  is the thermal softening coefficient.

The equation is constituted of three main terms:

- The elasto-plastic term which depends on the strain of the material and represented by  $[A + B(\varepsilon_p)^n]$ .
- The viscosity term which depends on velocity of displacement and represented by  $\left[ 1 + C * \ln \left( \frac{\dot{\varepsilon}}{\dot{\varepsilon}_0} \right) \right]$ .
- The thermal softening term which depends on temperature variation and represented by  $\left[ 1 - \left( \frac{T - T_{ref}}{T_{melt} - T_{ref}} \right)^m \right]$ .

The tensile tests data that were obtained at different temperatures and strain rates will be utilized to determine the constant parameters in the above three terms.

At the beginning, a reference strain rate and temperature need to be defined in order to follow the correct path in determining the parameters. In this case, a strain rate of  $0.0015 \text{ s}^{-1}$  will be the reference strain rate and the room temperature will be considered as the reference temperature.

### **3.3.1.1 Constants A, B, and n.**

The constants  $A$ ,  $B$ , and  $n$  are obtained using the true stress true strain curve produced from the tensile test at a reference strain rate of  $0.0015 \text{ s}^{-1}$  and a reference temperature of  $298 \text{ K}$  ( $25 \text{ }^\circ\text{C}$ ). By using the test data at these specific strain rate and

temperature, we can simplify the Johnson-Cook equation leading to have the viscosity term and thermal softening term equal to 1 as follows:

$$\sigma = [A + B(\varepsilon_p)^n] \quad (14)$$

The constant A corresponds to the yield point on the true stress true strain curve at which the plastic strain is zero. After determining the constant A, the remaining stresses are utilized to determine the strain hardening parameters B and n.

### 3.3.1.2 Constant C.

Constant C is the strengthening coefficient in JC model. This constant is obtained using the tensile test results produced from the three different strain rates of 0.0015, 0.015, and 0.15  $s^{-1}$  at the reference temperature of 298 K (25 °C). By using the tests results at reference temperature, we can simplify the Johnson-Cook equation leading to have the thermal softening term equal to 1. Since constants A, B, and n are known at this stage, the JC equation can be rearranged to be:

$$\frac{\sigma}{[A+B(\varepsilon_p)^n]} - 1 = C * \ln\left(\frac{\dot{\varepsilon}}{\dot{\varepsilon}_0}\right) \quad (15)$$

The term  $\frac{\sigma}{[A+B(\varepsilon_p)^n]} - 1$  is denoted as  $\sigma_c$  afterwards will be evaluated at yield strain, 1% strain, 2% strain, 10% strain, and 20% strain using the data for the three different strain rates. The values of  $\sigma_c$  against the three constant values of  $\ln\left(\frac{\dot{\varepsilon}}{\dot{\varepsilon}_0}\right)$  at the three strain rates of 0.0015, 0.015, and 0.15  $s^{-1}$  will then be plotted. Since the  $\ln\left(\frac{\dot{\varepsilon}}{\dot{\varepsilon}_0}\right)$  values are constant for all strain levels, the relationship between  $\ln\left(\frac{\dot{\varepsilon}}{\dot{\varepsilon}_0}\right)$  and  $\sigma_c$  will be almost linear. Therefore, the slope of each line at these strain levels will be calculated and the constant C will be the average of these slopes.

### 3.3.1.3 Constant m.

The thermal constant m characterizes is the effect of temperature in JC model. This constant can be obtained using the data produced from the tensile test at specific strain rate and different temperatures. Usually, the data used to obtain constant m is taken from the tensile test at reference strain rate. However, and as will be shown in

later sections, due to the strain aging happening in wide region at the reference strain rate with higher temperatures, using these data will give inaccurate results. Therefore, and since constant C is known at this stage, the data from the tensile tests at strain rate of  $0.15 \text{ s}^{-1}$  and temperatures of 523 K, 723 K, and 923K were considered. Detailed analysis of the strain aging will be addressed in the next chapter. Moreover, since the values of constants A, B, n, and C are known at this stage, we can simplify the Johnson-Cook equation to be as follows:

$$\frac{\sigma}{[A+B(\varepsilon_p)^n][1+C*\ln(\frac{\dot{\varepsilon}}{\dot{\varepsilon}_0})]} = 1 - \left( \frac{T-T_{ref}}{T_{melt}-T_{ref}} \right)^m \quad (16)$$

Rearranging the equation will lead to have:

$$\ln \left( 1 - \frac{\sigma}{[A+B(\varepsilon_p)^n][1+C*\ln(\frac{\dot{\varepsilon}}{\dot{\varepsilon}_0})]} \right) = m \ln \left( \frac{T-T_{ref}}{T_{melt}-T_{ref}} \right) \quad (17)$$

The term  $1 - \frac{\sigma}{[A+B(\varepsilon_p)^n][1+C*\ln(\frac{\dot{\varepsilon}}{\dot{\varepsilon}_0})]}$  denoted as  $\sigma_m$  will be evaluated at yield strain, 1% strain, 2% strain, and 10% strain using the data for the three different temperatures at strain rate of  $0.15 \text{ s}^{-1}$ . Afterwards, the values of  $\ln \sigma_m$  against the three constant values of  $\ln \left( \frac{T-T_{ref}}{T_{melt}-T_{ref}} \right)$  at the three temperatures of 523 K, 723 K, and 923K will be plotted. Since the  $\ln \left( \frac{T-T_{ref}}{T_{melt}-T_{ref}} \right)$  values are constant for all strain levels, the relationship between  $\ln \left( \frac{T-T_{ref}}{T_{melt}-T_{ref}} \right)$  and  $\sigma_m$  will be almost linear. Therefore, the slope of each line at these strain levels will be calculated and the constant m will be the average of these slopes.

### 3.3.2 Energy based damage model parameters.

As explained earlier, Abed et al. [10] developed an energy based model that is capable of describing the damage evolution in steel using the principles of continuum damage mechanics.

The model describes the damage as the increase in the dissipated energy of the material. In other words, the material ability to absorb energy will reduce during the

loading process until it reaches failure where it will not be able to absorb energy afterwards. The concept is illustrated in Figure 16.

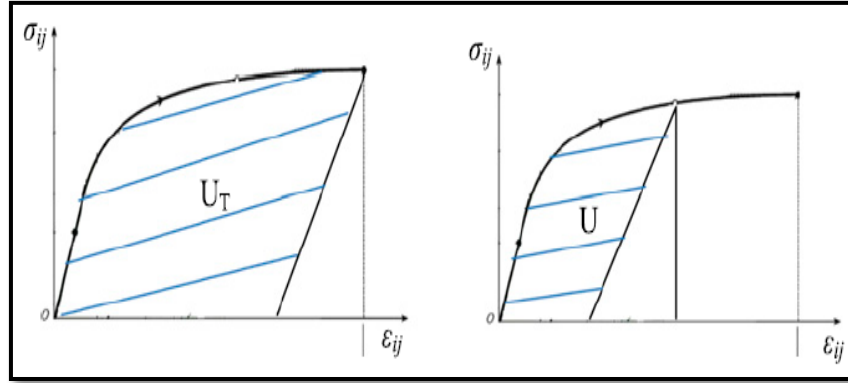


**Figure 16: Illustration of the model concept [10]**

As shown in Figure 16, the damage resulting from the elastic deformation is very small compared to the damage resulting from the accumulation of the plastic deformation. Therefore, the model assumes that it is reasonable to neglect the damage resulting from the elastic deformation, and it considers that the damage initiates with the initiation of plastic deformation.

The model is expressed as a function of the dissipated energy ratio to the total dissipated energy and the damage at fracture as shown in equation (18):

$$\Phi = \Phi_f \left( \frac{U_p}{U_{PT}} \right)^\alpha \quad (18)$$

Where  $\Phi$  is the damage at the point of interest during the deformation process,  $\Phi_f$  is the damage at fracture which is measured using SEM images,  $U_p$  is the corresponding dissipated energy at this point of interest,  $U_{PT}$  is the total dissipated energy, and the exponent  $\alpha$  is the constant that determines the trend of damage evolution throughout the deformation process. Since most steel tend to have similar trend for the damage evolution throughout the deformation process, the value of the exponent  $\alpha$  for C45 steel is assumed to be similar to the one indicated by Abed et. al. [10].

The dissipated plastic energy can be determined using equation (19), where  $\sigma$  and  $\varepsilon$  are the true stress and true strain, respectively

$$U_p = \int_0^{\epsilon^p} \sigma d\epsilon^p \quad (19)$$

### **3.4 Phase Four: Coupled Damage-Plasticity Constitutive Modeling**

The coupling effect of damage and plasticity will be studied in this phase by integrating the energy based damage model into the JC model to accurately capture the stress strain behavior of C45 steel. This will be done using equation (2) as previously discussed in Chapter 2. In this case, the effective stress will be calculated using the JC relationship described in equation (13) and the evolution of damage will be determined according to equation (18).

### **3.5 Phase Five: Finite Element Simulation**

The main objective of this phase is to simulate the same experimental scenarios using the finite element software ABAQUS in order to verify the results of the JC model. The software ABAQUS was chosen because of its capabilities to conduct nonlinear analysis and simulate different loading scenarios. Moreover, the JC model is already implemented in ABAQUS and therefore, no need to numerically integrate the constitutive equations into the finite element code.

First, verification of the JC model parameters will be performed by simulating a simple uniaxial axisymmetric tensile specimen as shown in Figure 17. Due to symmetry, a quarter of the specimen will be considered with a mesh of one element. Model verification will be compared with all experimental loading cases.

Afterwards, finite element modeling will be extended to simulate quasi-static tests and drop hammer experiments using the verified JC model parameters. The details of the simulation along with the results obtained are addressed and discussed in Chapter 5.

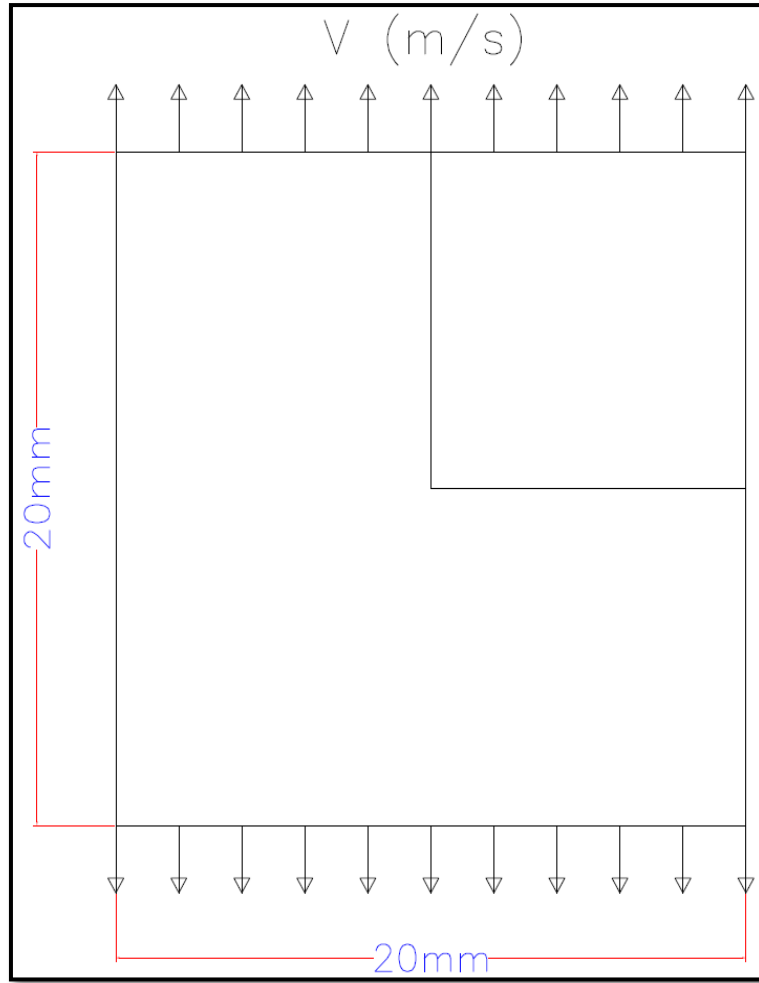


Figure 17: Simple axisymmetric element subjected to tensile loading rate

## Chapter 4 : Experimental Tests, JC Model, and Energy Damage Model

### Results and Discussions

#### 4.1 Tensile Tests

Quasi-Static tests with three different rates of deformation were performed on C45 structural steel at room and high temperatures. The resulting measured stresses and strains were recorded and converted into true stresses and true strains respectively. The true stress-true strain curves for tensile tests at room temperature and strain rates of  $0.0015\text{s}^{-1}$ ,  $0.015\text{s}^{-1}$ , and  $0.15\text{s}^{-1}$  are shown in Figure 18.

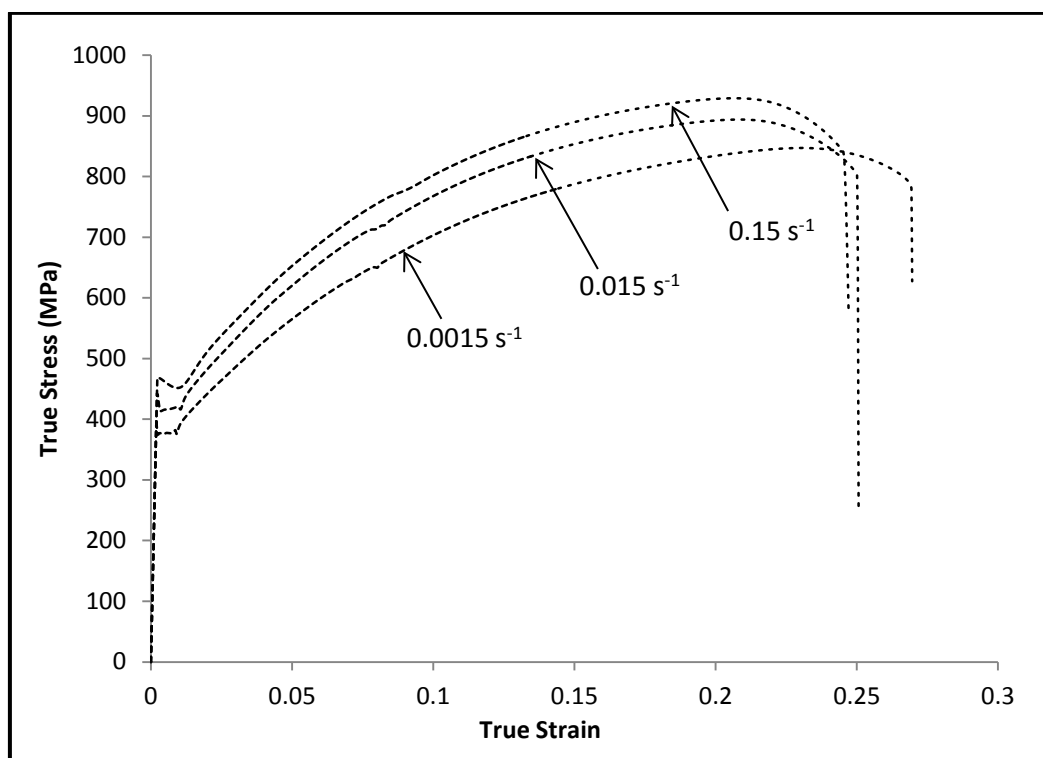
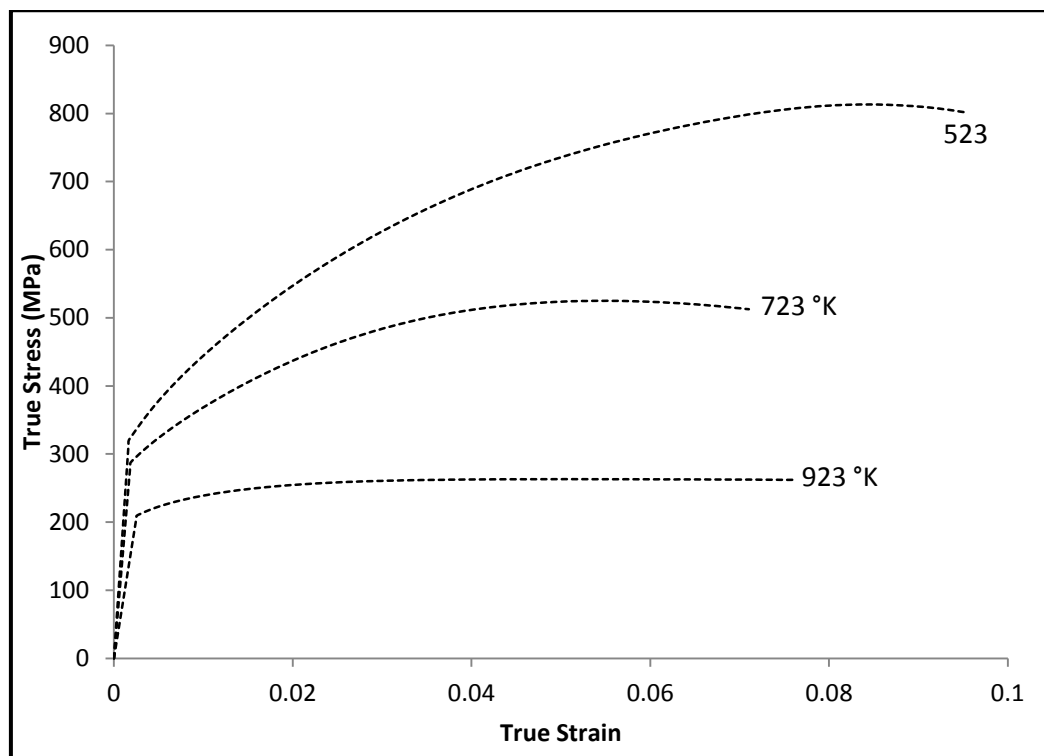


Figure 18: True stress-true strain curves at room temperature for different strain rates

As shown in Figure 18, the yield stresses along with the ultimate stresses are increasing with the increase of the strain rate. This is a typical trend of steel in general and high strength steel in specific. Also, the point of fracture is happening at lower strains with the increase of strain rate. With the increase of strain rate, the loads are increasing but the time taken to apply these loads is the same. Thus, more strain energy density is getting absorbed by the material at constant time of load application. When the material absorbs energy, it increases the stress induced within the

microstructure of the material leading to have higher stress values at the same strain. Accordingly, the material will reach its maximum capacity of energy absorption at earlier point. This explains why with the increase of strain rate, the yield and ultimate point are increased and why the fracture happens at earlier point of strain.

Despite the above mentioned, it can be noticed that the trend of the stress strain curve is similar regardless of the values achieved. In other words, the main difference is the yield point and the point of fracture. If the yield point is the same, the curves will be almost identical. The increase in yield stress is interpreted physically as the resistance of initial dislocation by the “Peierls barriers provided by the lattice itself.” This indicates that the “viscous-thermal” part of the flow stress at room temperature is mainly controlled by the yield stress and nearly independent of the plastic strain [72]. The quasi-static tensile tests were extended to investigate the mechanical response of C45 steel at higher temperatures. For that purpose, three temperatures of 523 °K, 723 °K, and 923 °K at two quasi-static loading rates were considered. The true stress-true strain curves for these high temperature tests are shown in Figures 19 and 20 for strain rates of  $0.0015\text{s}^{-1}$  and  $0.15\text{s}^{-1}$ , respectively.



**Figure 19: True stress-true strain curves at high temperatures for strain rate of  $0.0015\text{s}^{-1}$**

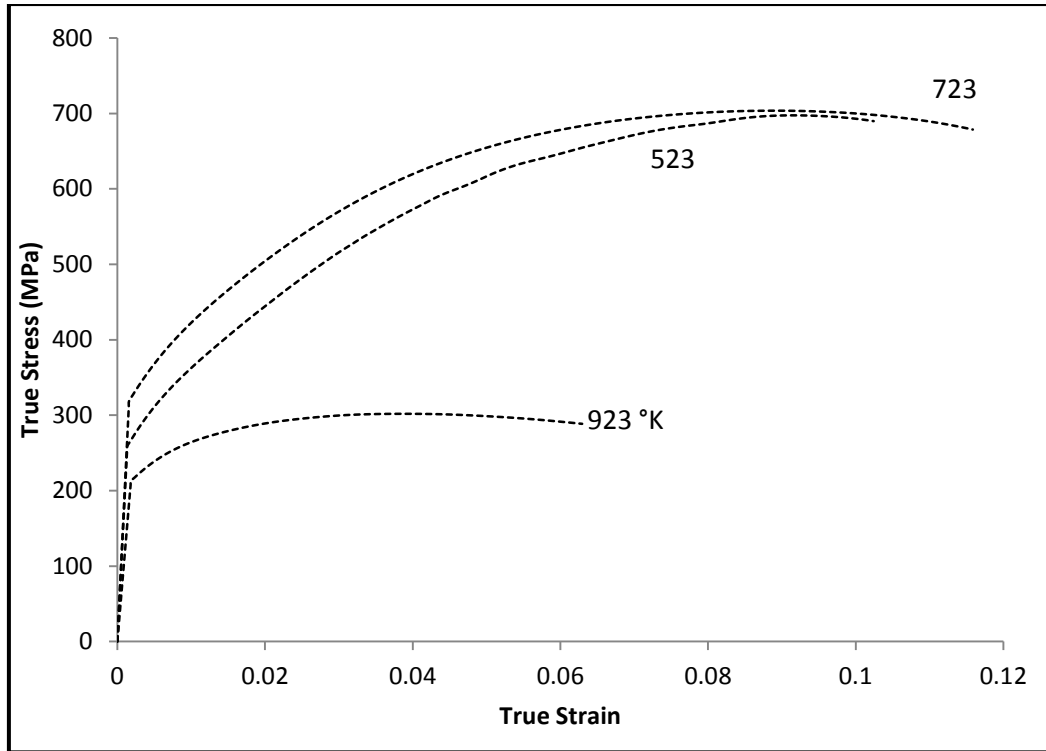


**Figure 20: True stress-true strain curves at high temperatures for strain rate of  $0.15s^{-1}$**

The yield point of metals in general is not easily determined at elevated temperatures as compared to the case for room temperature. For that reason, the determination of the yield stress of metals at high temperatures has been identified differently by various design codes. According to Wang et al. [85], the European Convention for Constructional Steelwork [86] and the AISC [87] identify the yield point at the nominal strain level of 0.5% for temperature exceeding 400 °C. Also, it identifies the yield point as the interpolation between 0.2% offset and 0.5% nominal strain for temperatures between 25 °C and 400 °C. On the other hand, the BS5950 [88] code defines the yield point at nominal strains of 0.5%, 1.5%, or 2%. As for EC3 [89] and Eurocode 4 [90], it is defined at 0.2% strain offset. After investigating all the aforementioned approaches, the EC3 and Eurocode 4 approach was adopted in this research in which the yield point was defined at 0.2% offset.

It can be noticed from Figure 19 for strain rate of  $0.0015s^{-1}$  that the stresses are generally decreasing with the increase of temperature. However, the difference between the ultimate stresses at temperatures of 523 °K and 723 °K is much more than that at temperatures 723 °K and 923 °K, with the yield stresses that are close to each other at temperatures of 523 °K and 723 °K. Also, the plastic region at

temperature of 923 °K is almost flat, which indicates that the strain hardening at this high temperature level is diminished, and the remaining are denoted as athermal stresses [28, 32, 72, 73]

The same observations can be made on the true stress-true strain curves shown in Figure 20 for thermal tensile tests performed at strain rate of  $0.15\text{s}^{-1}$ . However, it is clearly shown that the stresses for the specimen at temperature of 723 °K are higher than the stresses at 523 °K. Such a jump in the stress value is attributed to what is called the dynamic strain aging (DSA) phenomenon that is usually encountered in high strength ferrite and austenite steel and at different combinations of temperatures and strain rates.

According to Wang et al. [91], dynamic strain aging is basically a phenomenon that occurs due to the interaction between “diffusing solute atoms” and “mobile dislocations” in the material. It usually occurs after “critical strain” at specific “regime” of strain rate and temperature. The authors stated that the range of temperatures at which this phenomenon occurs is between 20% and 50% of the melting temperature. The effect of DSA can be expressed in the material as “serrated flow”, “negative strain rate sensitivity”, and “peaks or plateaus on flow stress/temperature plots.”

The DSA behavior can be clearly noticed when the stresses variations with temperature are plotted for different strain levels as shown in Figure 21 and Figure 22 for the lower and higher strain rates considered. The peaks/jumps in the flow stress are clearly noticed at temperature of 523 °K and partially at temperature 723 °K for strain rate of  $0.0015\text{s}^{-1}$  and at temperature of 723 °K for strain rate of  $0.15\text{s}^{-1}$ .

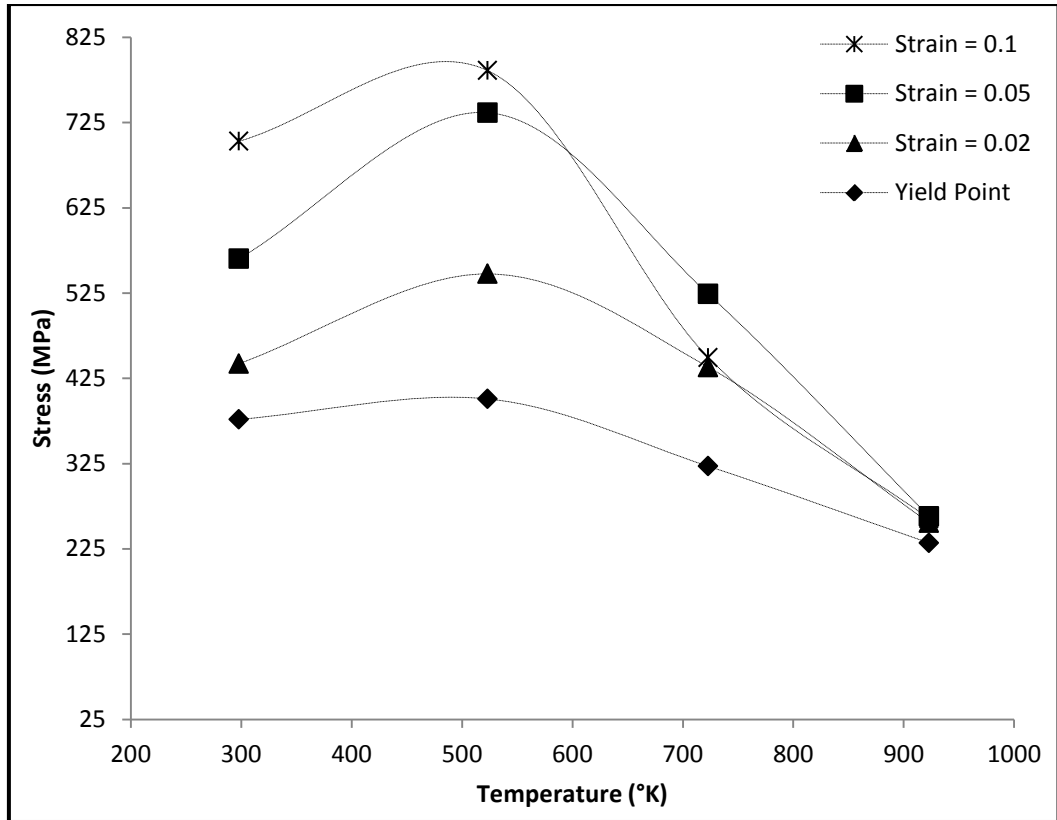


Figure 21: Stress variations against temperature for strain rate  $0.0015s^{-1}$  at various strain levels

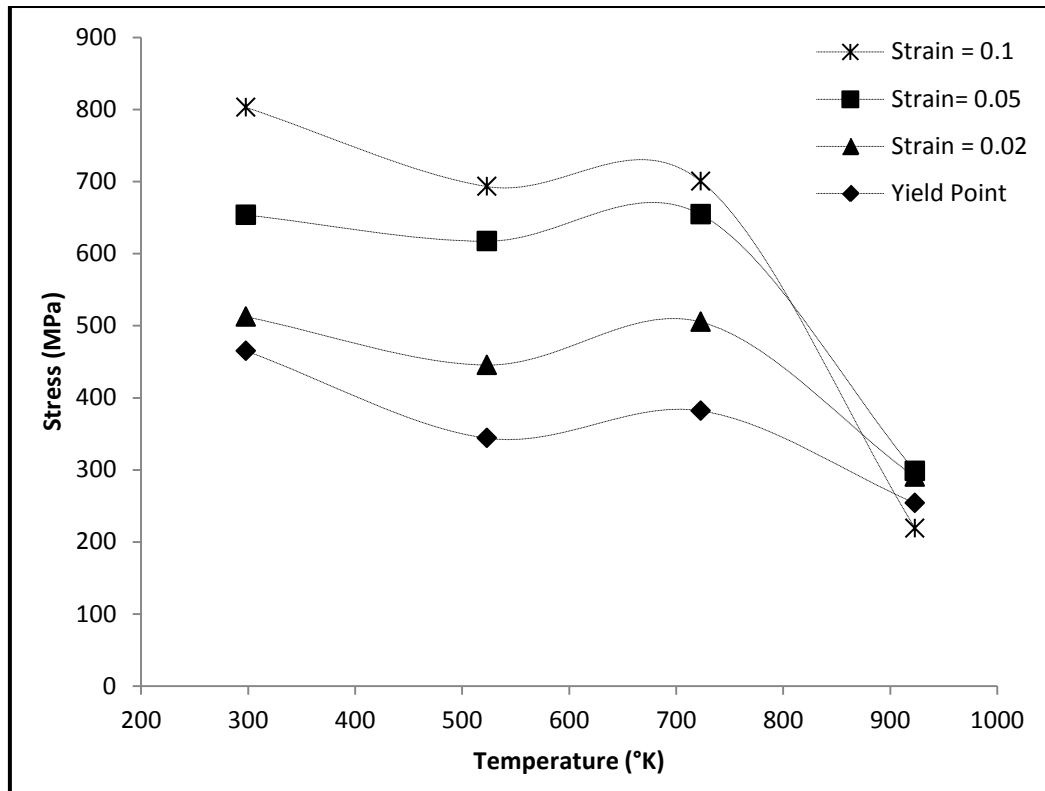
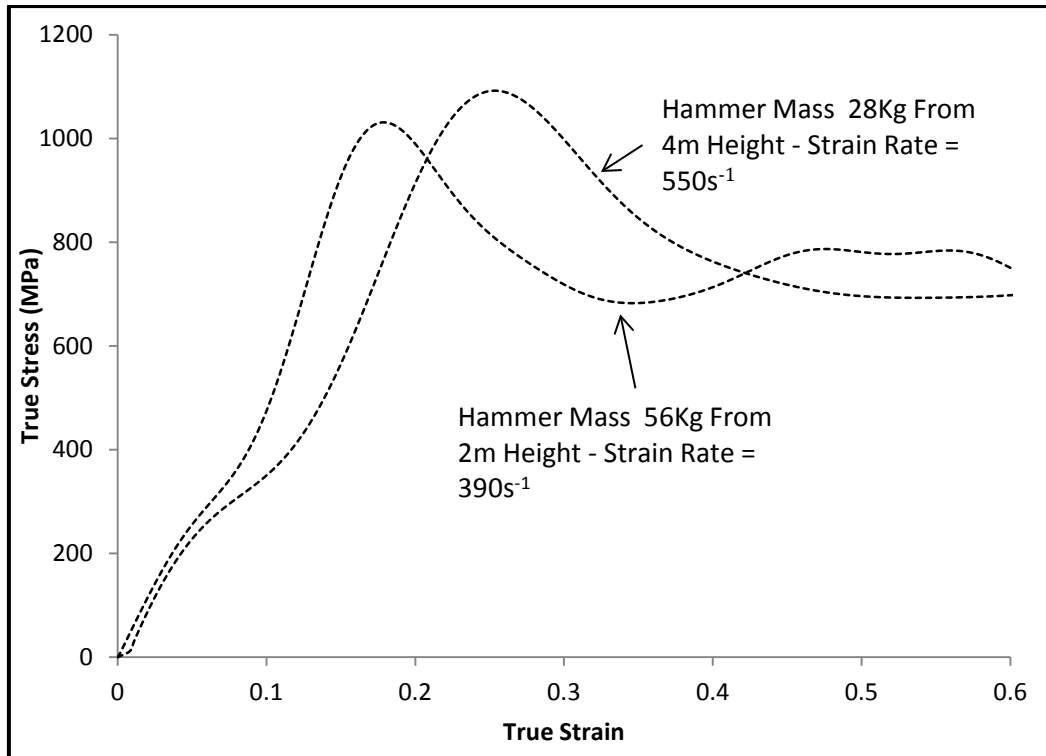


Figure 22: Stress variation against temperatures for strain rate  $0.15s^{-1}$  at various strain levels

## 4.2 Drop Hammer Test

Two Drop Hammer tests with strain rate equivalent to  $390\text{s}^{-1}$  and  $550\text{s}^{-1}$  were conducted on C45 structural steel at room temperature. The resulting measured strains and stresses have been recorded and converted to true strains and true stresses respectively. The true stress-true strain curves for both loading scenarios adopted in the experimental program explained earlier are shown in Figure 23.



**Figure 23:** True stress-true strain curves for drop hammer test at strain rates of  $390\text{s}^{-1}$  and  $550\text{s}^{-1}$

It is difficult to identify a clear point which defines the yield of the material at such high strain rate values. This can be clearly noticed in Figure 23 where the curves are increasing until they achieve the ultimate stress and then start to decrease until point of fracture. However, the trend of the two curves is similar regardless of the values achieved. Also, the main difference between both loading scenarios is the ultimate point achieved in which the ultimate stresses increased with the increase of the strain rate.

### 4.3 SEM Analysis and Damage Model Parameters

After implementing the procedure discussed earlier to measure the area of cracks at fracture using the ImageJ software [92], the results obtained are shown in Table 6. Sample images obtained using the SEM machine are shown in Figure 24 for strain rate of  $0.15\text{s}^{-1}$  at various temperatures.

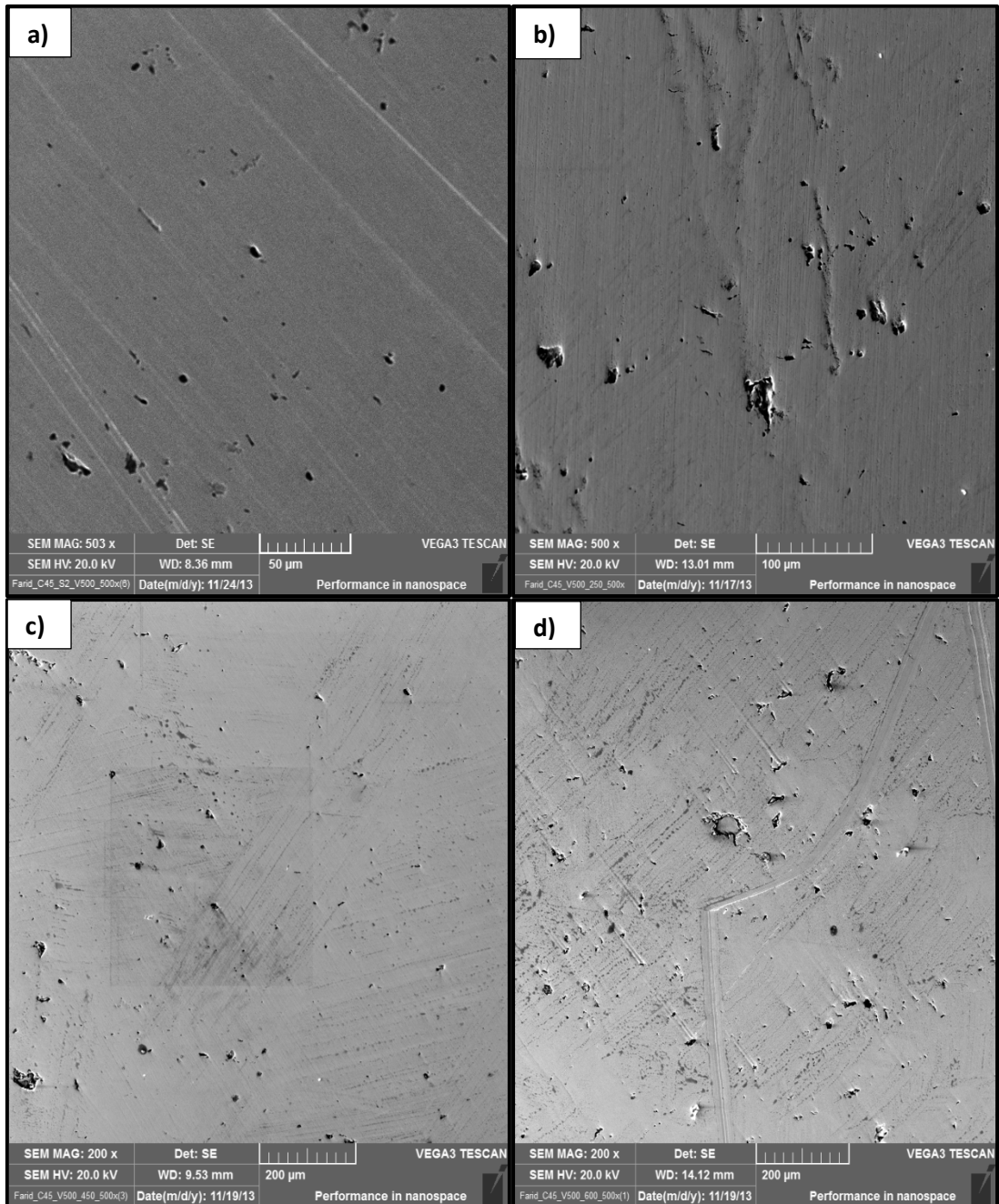


**Figure 24: SEM images of fractured damaged surfaces at different temperatures for strain rate of  $0.15\text{s}^{-1}$ , a)  $T = 298\text{ °K}$ , b)  $T = 523\text{ °K}$ , c)  $T = 723\text{ °K}$ , and d)  $T = 923\text{ °K}$**

**Table 6: SEM analysis results**

Temperature (°K)	Strain Rate	Damage $\Phi$ at Fracture
Room Temperature (298)	0.0015	0.05
	0.015	0.064
	0.15	0.09
523	0.0015	0.07
	0.15	0.11
723	0.0015	0.1
	0.15	0.15
923	0.0015	0.16
	0.15	0.21

The results shown in Table 6 are also illustrated in bar charts as shown in Figure 25, which clearly explains the increasing pattern of the damage values with the increase of temperature and strain rates. The results are reasonable since the higher the temperature and the strain rate, the higher the stress induced on the microstructure of the material. This will lead to form more micro-voids and cracks leading to more area lost within the microstructure of the material.

The results shown in Table 6 have been used in order to determine the energy based damage model parameters. As discussed earlier, the model is represented by equation (18), where the term  $\Phi_f$  is taken from the results shown in Table 6. The value of the constant  $\alpha$  which describes the trend of the damage evolution was assumed as 2.0 similar as obtained from [10].

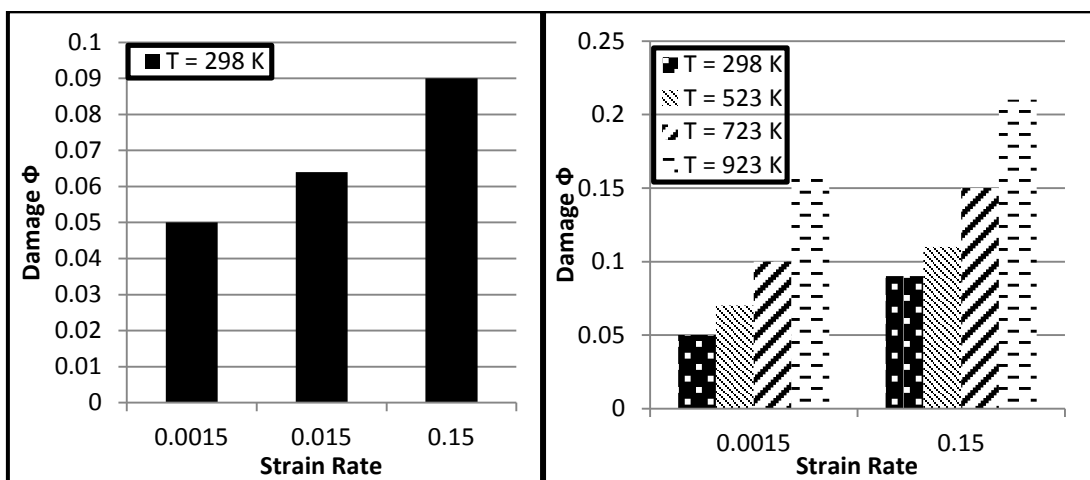


**Figure 25: Damage  $\Phi$  at fracture for each rate of deformation at all temperatures**

The damage evolution results for C45 steel are presented in Figure 26 for all loading combinations considered. The damage grows at a higher rate with the increase of strain rate except for the case at temperature 723 °K. This is because of the strain aging phenomenon that leads the material to gain more strength regardless of the temperature increase at higher rates. Also, the strain aging can be noticed affecting the damage evolution at a temperature of 523 °K. However, the damage still grows at a higher rate with the increase of the strain rate but with lesser difference than the room temperature and the 923 °K. Overall, the results seem to be reasonable and they seem to follow the trend that the high strength steel follows at these conditions [10].

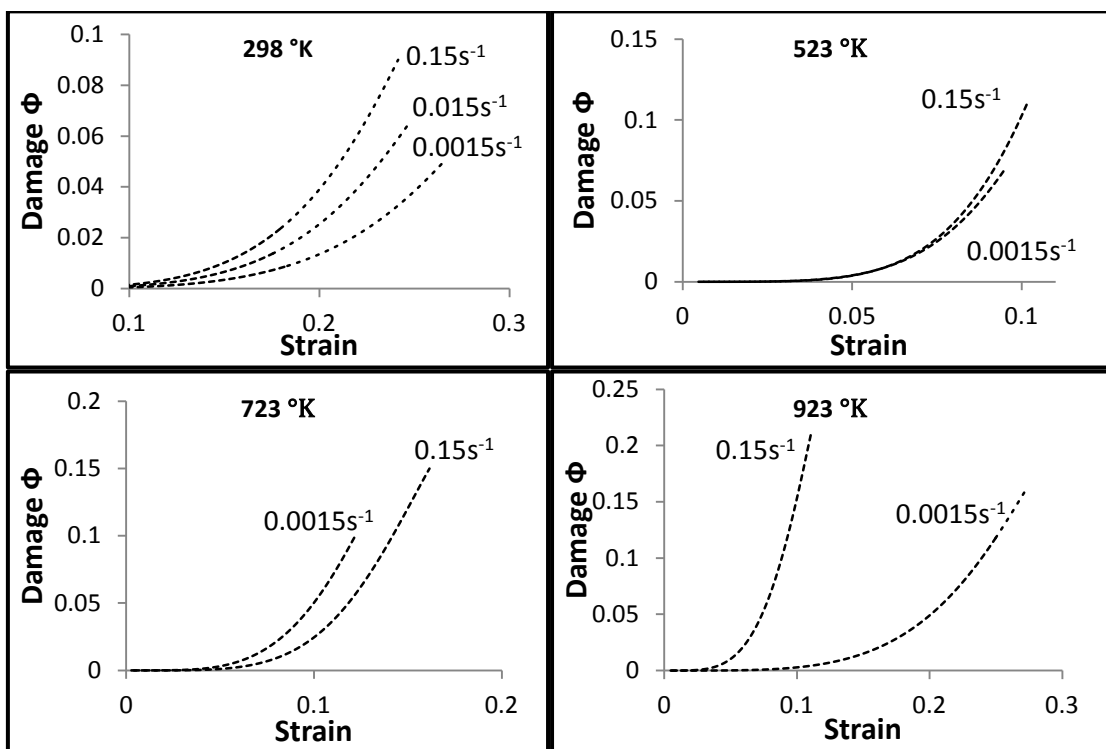


**Figure 26: Damage  $\Phi$  evolution in the material for different strain rates and temperatures**

It can be noticed from Figure 26 that the damage effect starts to grow on higher scale at a certain strain point for each case. At the beginning, the damage evolution is almost constant until a certain strain point at which the damage starts to grow faster, leading to the degradation of the material. This is because the dissipated plastic energy, which is represented by the area under the stress-strain curve, is increasing with strain until it reaches a value of high ratio compared to the total energy. At that point, the damage effect starts to be noticed clearly as shown in Figure 26. In a later section, the effect of the damage will be implemented in the suggested

constitutive model where the integration of the model will better simulate the degradation of the material as discussed here.

#### 4.4 JC Model Parameters

As mentioned previously, the constant A corresponds to the value of the yield point on the true stress true strain curve at a reference strain rate and a reference temperature). This value is estimated to be around 230 MPa. After determining the constant A and by using the regression analysis explained in Chapter 3, the values of  $B = 1260$  and  $n = 0.43$  were obtained using the experimental strain hardening results at the same reference temperature and strain rate.

Considering the above obtained strain hardening constants and using the experimental stress-strain results for different quasi-static loading rates, at room temperature only, the values of  $\sigma_c$  were plotted against  $\ln\left(\frac{\dot{\epsilon}}{\dot{\epsilon}_0}\right)$  as per equation (15) at the three strain rates of  $0.0015s^{-1}$ ,  $0.015s^{-1}$ , and  $0.15s^{-1}$ . Accordingly, the slope of each line at these strain levels was calculated and averaged to determine the constant value  $C = 0.030$ .

Finally, the constant  $m$  was determined after plotting the values of  $\ln \sigma_m$  as per equation (17) in Chapter 3 versus the three constant values of  $\ln\left(\frac{T-T_{ref}}{T_{melt}-T_{ref}}\right)$  at the three temperatures of 523 °K, 723 °K, and 923 °K and for different plastic strain levels. The slope of each line at these strain levels was calculated and the constant  $m$  was taken as the average of these slopes. Accordingly, the resulting average value of exponent  $m$  was around 0.9.

Based on the abovementioned constants identification procedure, the final form of the JC equation can be defined as follows:

$$\sigma = \left[230 + 1260(\epsilon_p)^{0.43}\right] \left[1 + 0.030 * \ln\left(\frac{\dot{\epsilon}}{\dot{\epsilon}_0}\right)\right] \left[1 - \left(\frac{T-T_{ref}}{T_{melt}-T_{ref}}\right)^{0.9}\right] \quad (20)$$

The temperature and strain rate variations trends of the flow stresses for C45 steel predicted using JC model (equation 20) was initially verified by direct comparisons with experimental results. Figures 27 and 28 compare the stress variation

with temperature predicted using equation (20) with their experimental results counterpart. In general, the JC model shows acceptable comparisons at certain strain values and realistically captures the nonlinear trend of C45 steel over the range of temperatures and strain rates considered. However, some deviation can be noticed in regions where the strain aging is active. According to Voyiadjis and Abed [93], the DSA effect becomes active when the aging time is equal to the waiting time of mobile dislocations which in turn increases the obstacle strength by certain amount (i.e., jump). Therefore, in order to predict this stress increase, an additional mathematical expression involving the DSA physical characterization is required. For this reason, it is fair to say that the C45 material constants obtained in this study for the JC model is more applicable at room temperature conditions. This is confirmed by the good comparison shown in Figure 29 between the JC model predictions and experimental results at room temperature for different strain rates. Therefore, the finite element simulations presented in the next chapter will be focused on simulating experimental tests at room temperature only.

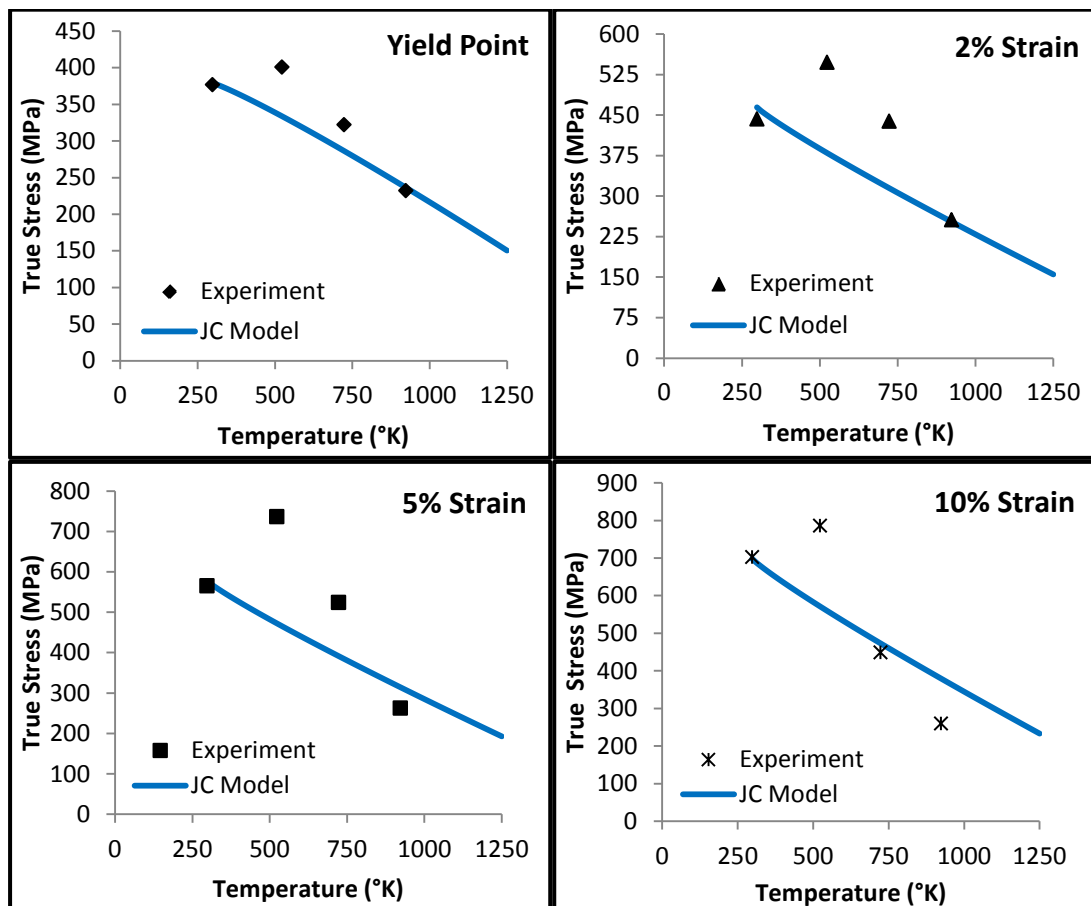


Figure 27: Temperature vs stress at different strain levels for strain rate of  $0.0015s^{-1}$

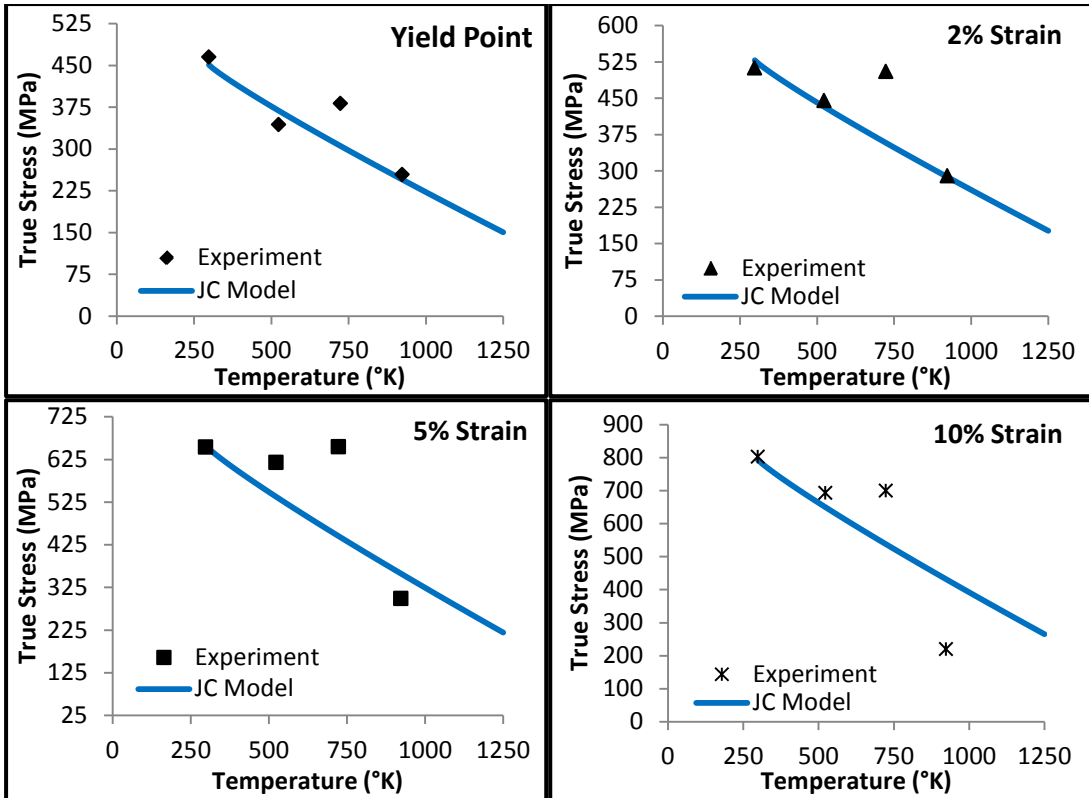


Figure 28: Temperature vs stress at different strain levels for strain rate of  $0.15s^{-1}$

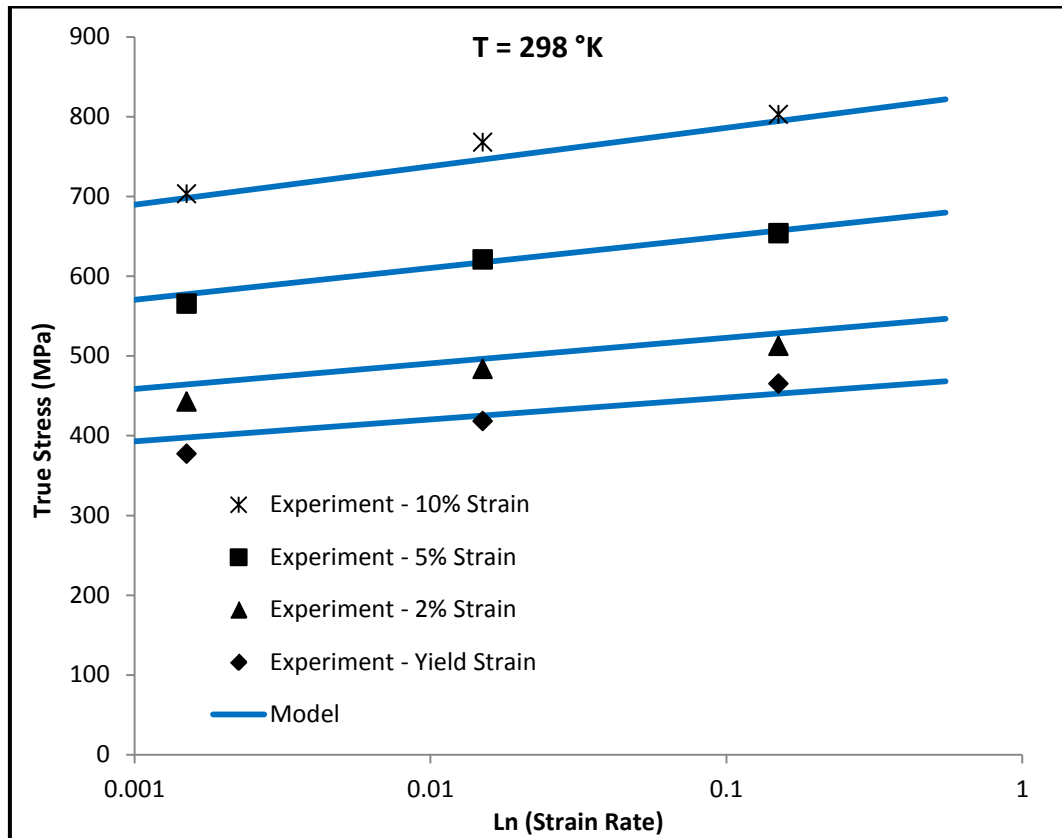


Figure 29: Strain rate vs stress at different strain levels for temperature of  $298 \text{ } ^\circ\text{K}$

## Chapter 5 : Finite Element Simulation

The main objective of the finite element (FE) simulation presented in this chapter is to verify the applicability of JC model and energy-based damage model to simulate the same experimental coupon and drop hammer tests. The FE modeling was conducted using ABAQUS 6.14 [94] and was limited to experiments conducted at room temperatures but under different quasi-static and dynamic loadings. Three different FE models were developed to achieve the above objective. The first FE model considers a simple one element axisymmetric problem to verify the accurate implementation of the coupled JC-damage model and its capability to reproduce the experimental stress strain curves at the range of temperatures and strain rates discussed earlier. The second problem is concerned with simulating the quasi-static tensile tests that were performed in the experimental program at room temperature only. As for the third problem, the drop hammer test is simulated and compared with the experimental results.

### 5.1 Simple One-Element Axisymmetric Test

A simple one-element uniaxial tensile test is considered to validate the finite element implementation of the coupled damage-JC model prior to simulating any other problems. For that purpose, the axisymmetric one-element model was subjected to the same range of temperatures and loading rates adopted in the experimental program. As shown in Figure 17, the dimensions considered for this analysis was 20mm of both sides of the element. Only quarter of the problem is considered in the analysis due to symmetry with restriction of displacement in the x-axis direction for the left side and in the y-axis direction for the bottom side of the element. Instantaneous loading profiles in terms of three velocities equal to  $1.5 \times 10^{-5}$  m/s,  $1.5 \times 10^{-4}$  m/s, and  $1.5 \times 10^{-3}$  m/s were applied to ensure strain rates of  $0.0015s^{-1}$ ,  $0.015s^{-1}$ , and  $0.15s^{-1}$ , respectively. The JC material constants used in this analysis are listed in Table 7 and the description of the problem is shown in Figure 30.

**Table 7: JC parameters implemented into the finite element simulation**

Parameter	$\epsilon_o$ ( $s^{-1}$ )	$T_{ref}$ ( $^{\circ}K$ )	$T_{melt}$ ( $^{\circ}K$ )	A (MPa)	B (MPa)	n	C	m
Value	0.0015	298	1793	230	1260	0.43	0.03	0.9

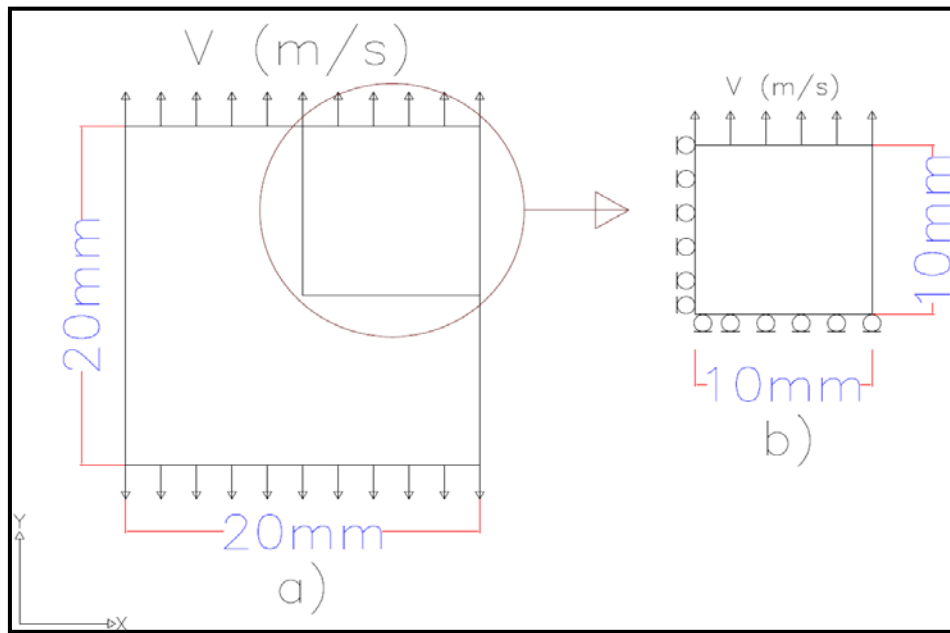


**Figure 30: Simple axisymmetric problem description: a) Cylindrical specimen subjected to loading. b) Quarter of the cylindrical specimen with boundary conditions**

The step time of the simulation was defined as per the time needed during the experimental tests for the material to fail. Finally, a predefined temperature of the same value as the experimental tests scenarios were considered and defined in the initial time step of the simulation. It should be mentioned that the adiabatic heat effect is included in the analysis for high strain rates of  $0.15\text{s}^{-1}$  only. For this purpose, the inelastic heat friction coefficient of value 0.1 and specific heat of value  $500\text{ J/Kg.K}$  are defined in the material parameters [72].

After setting up the model, the analysis was submitted to obtain the uniaxial stress-strain results. The element with its deformed shape is illustrated in Figure 31 for a selected case scenario. Figure 32 shows a very good comparison at room temperature between the stress-strain results predicted by the JC model and experiments. The coupled JC-Damage model was capable to predict the values and trends of the stresses up to fracture for the three different loading rates. On the other hand, the model was unable to capture the dynamic strain aging phenomenon encountered at temperatures of  $523\text{ °K}$  and  $723\text{ °K}$  as clearly shown in Figures 33 to 34. As mentioned earlier, dynamic strain aging phenomenon is a very complicated

process and; therefore, a physical-based constitutive term that is able to capture this increase in strength at the microstructural level is required. Despite that, the results shown are promising and the present JC model can be considered efficient to model the material response particularly at room temperature.

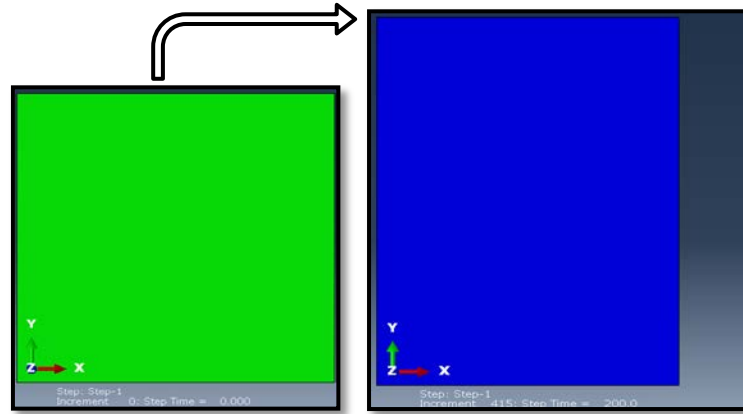


Figure 31: ABAQUS model of the one-element before and after deformation a loading scenario of strain rate =  $0.0015\text{s}^{-1}$  and  $T = 298\text{ }^\circ\text{K}$ .

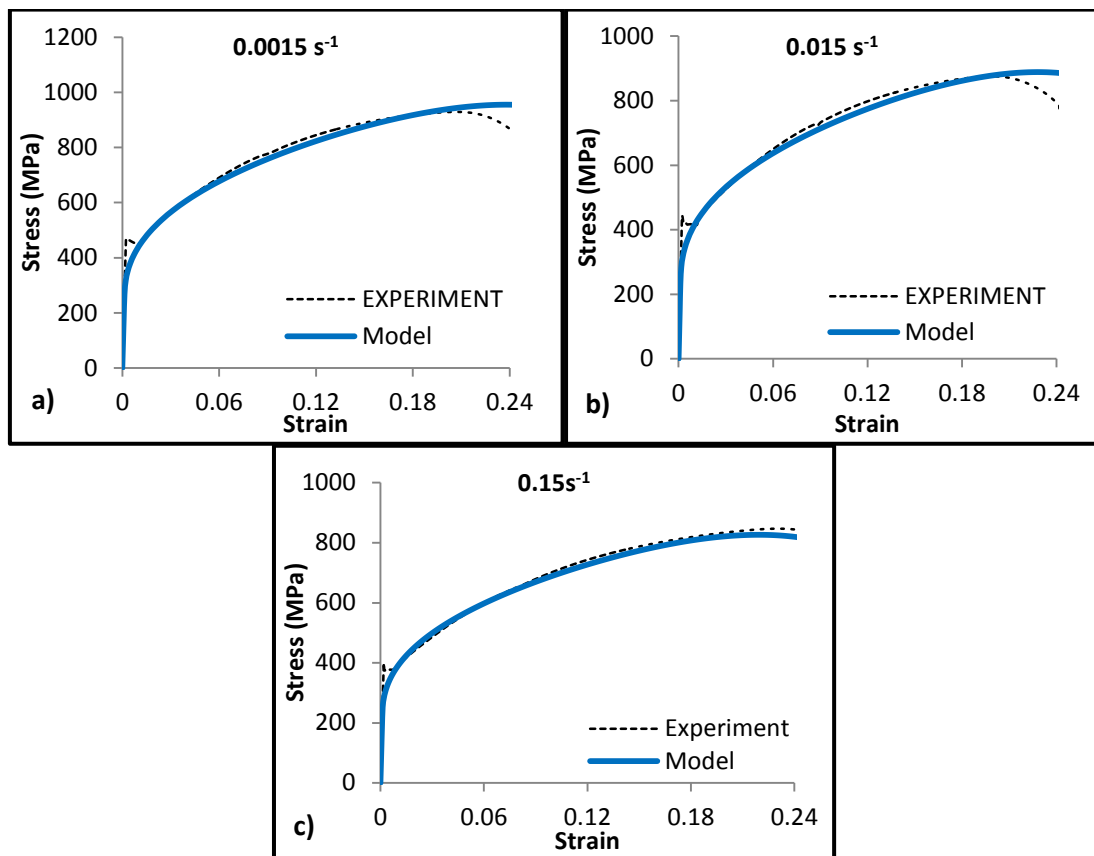


Figure 32: Stress-strain curves at  $T = 298\text{ }^\circ\text{K}$  for strain rates of a)  $0.0015\text{s}^{-1}$ , b)  $0.015\text{s}^{-1}$ , and c)  $0.15\text{s}^{-1}$

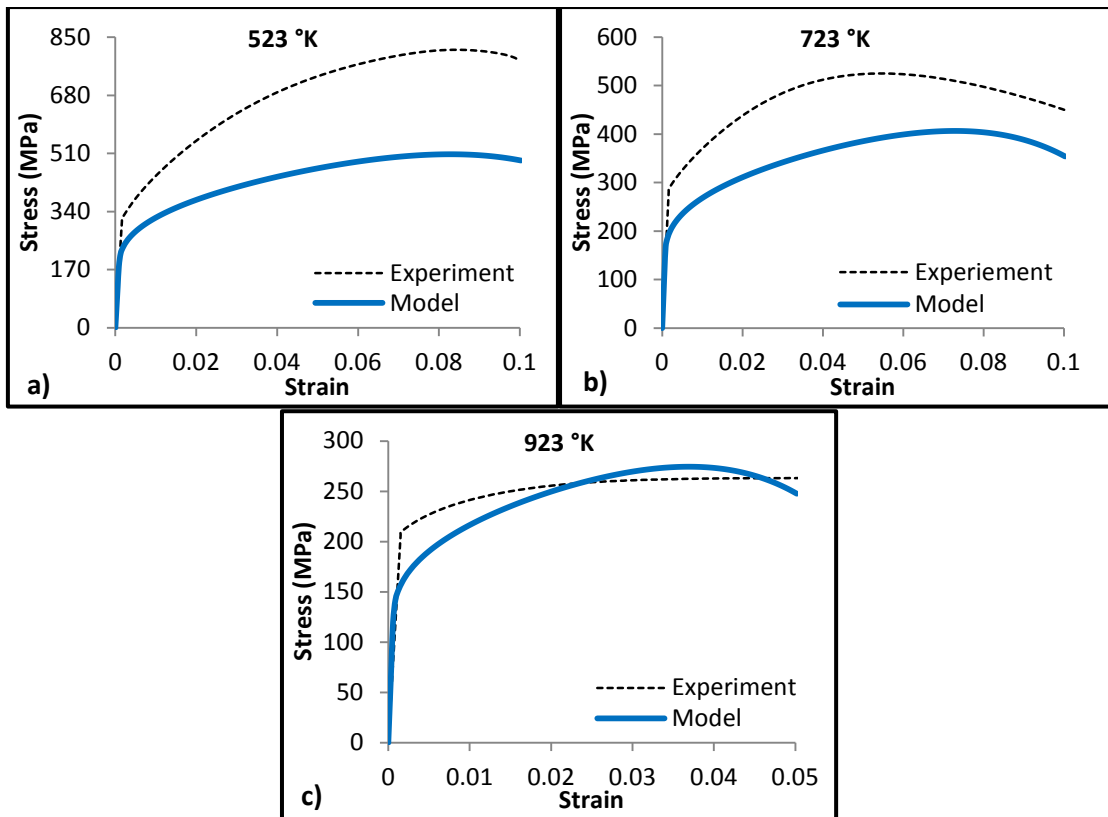


Figure 33: Stress-strain curves for strain rate  $0.0015\text{s}^{-1}$  at a)  $T = 523\text{ °K}$ , b)  $T = 723\text{ °K}$ , and c)  $T = 923\text{ °K}$

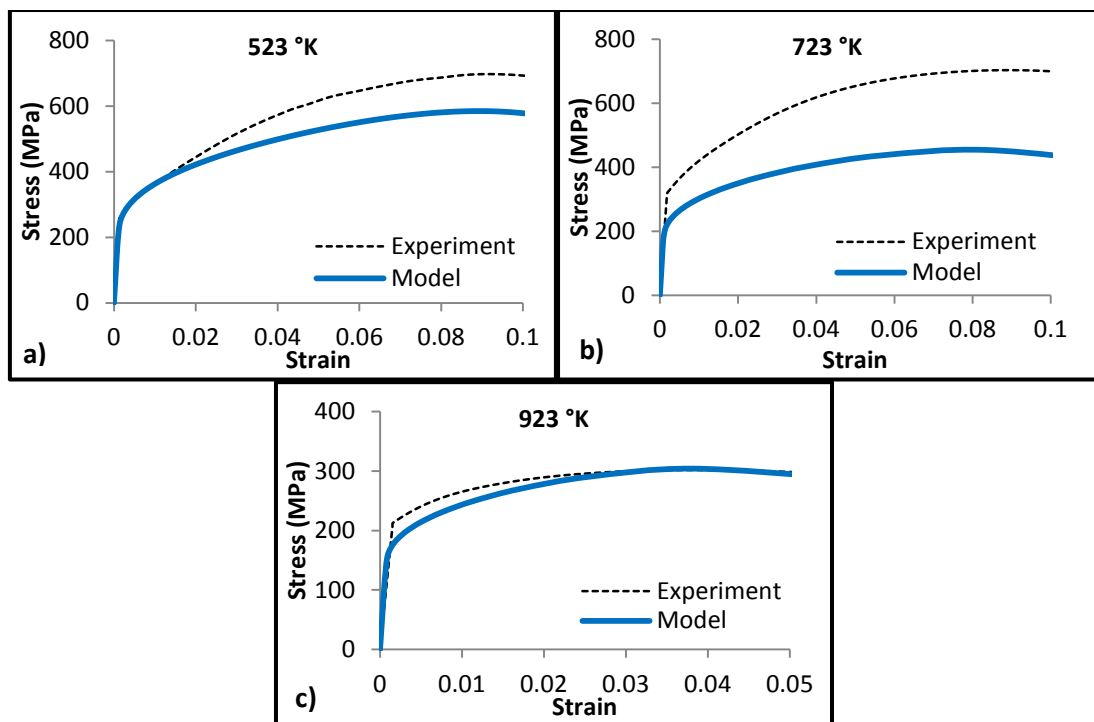


Figure 34: Stress-strain curves for strain rate  $0.15\text{s}^{-1}$  at a)  $T = 523\text{ °K}$ , b)  $T = 723\text{ °K}$ , and c)  $T = 923\text{ °K}$

### 5.1.1 Effect of damage.

This section is intended to show an example of the effect of including the energy-based damage evolution on the overall stress-strain response by comparing the experimental results with JC model prediction with and without including the damage model. For the comparison to be fair, it has to be between loading scenarios where the model captured the behavior almost successfully; in other words, for loading scenarios that are not affected by the dynamic strain aging phenomenon. Hence, loading scenarios at room temperature and 923 °K for loading rates of  $0.0015\text{s}^{-1}$  and  $0.15\text{s}^{-1}$  were considered in this comparison as shown in Figure 35.

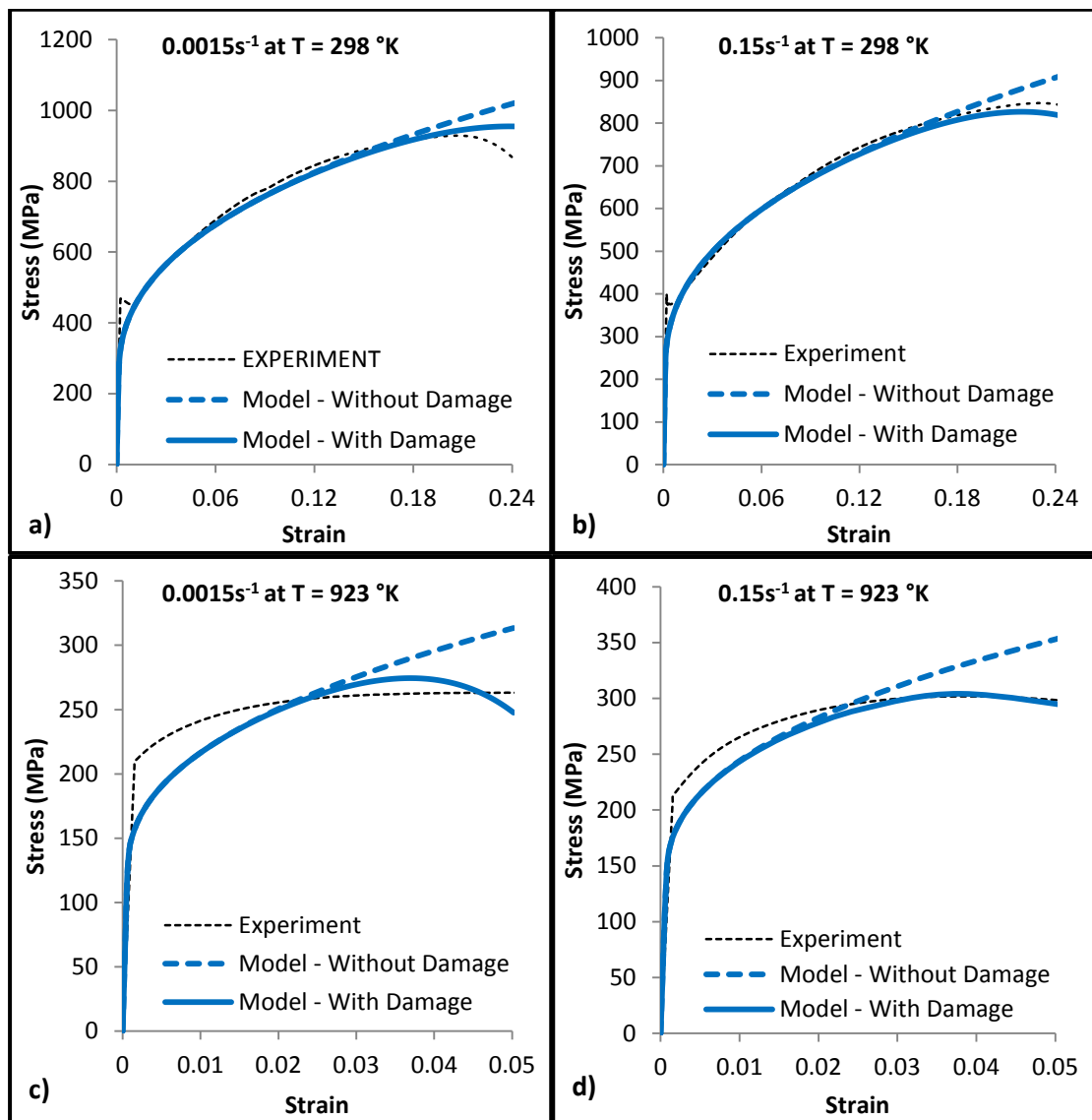


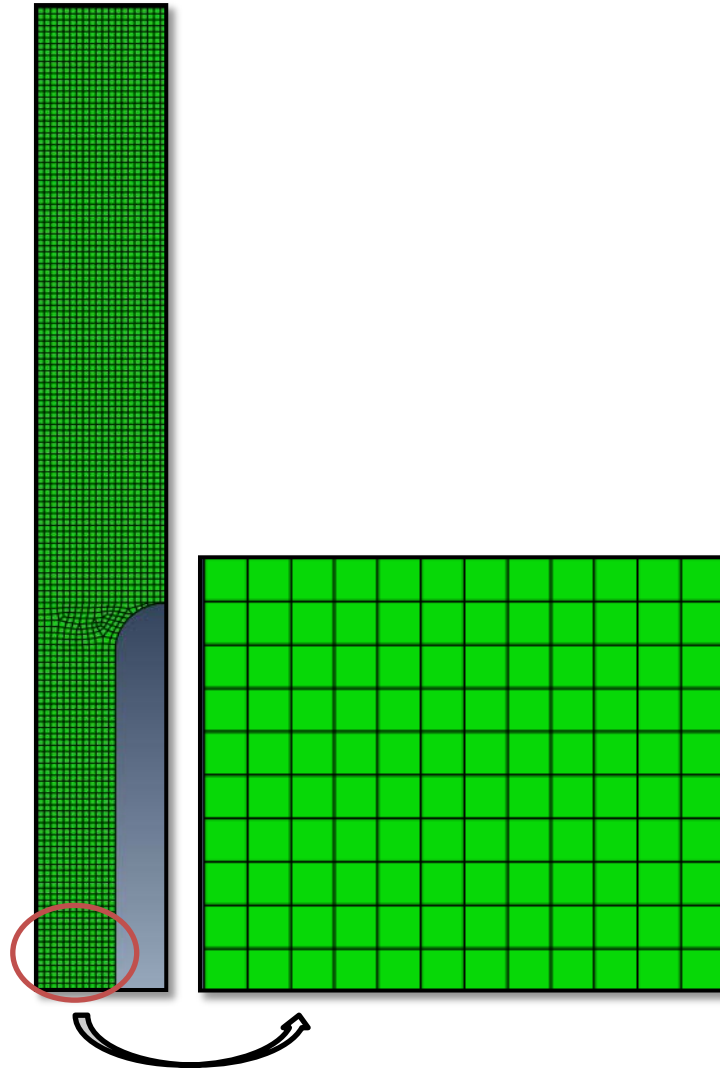
Figure 35: Comparison between experimental results, JC model, and coupled plasticity-damage JC model for a) Strain rate =  $0.0015\text{s}^{-1}$  at  $T = 298\text{ °K}$ , b) Strain rate =  $0.15\text{s}^{-1}$  at  $T = 298\text{ °K}$ , c) Strain rate =  $0.0015\text{s}^{-1}$  at  $T = 923\text{ °K}$ , d) Strain rate =  $0.15\text{s}^{-1}$  at  $T = 923\text{ °K}$

Figure 35 is clearly showing how the integration of the energy based damage model into the JC equation succeeded in capturing the failure mode in the material behavior. The JC model without including the damage is increasing without failure while including the damage has captured the fracture mode in the material for different loading scenarios. Overall, the application of the present model shall be only limited to room temperature. It needs to be verified with more experimental data to be verified for higher temperatures.

## 5.2 Quasi-Static Test Simulation

The verified and validated JC model was then utilized to simulate the quasi-static tensile tests at room temperature in order to further explore the accuracy of the present modeling. Due to the strain aging phenomenon, the quasi-static tests conducted at high temperatures will not be simulated.

As shown earlier, the quasi static tensile tests performed at room temperature were conducted using coupon specimens with rectangular cross-sections as shown in Figure 7. Due to symmetry, only a quarter of the specimen was modeled using the same dimensions listed in Table 3 for the experimental program. Plane stress elements of size 0.001, were considered in the FE simulation with a uniform mesh configuration throughout the specimen as shown in Figure 36. A displacement-control loading was applied at one end of the specimen in terms of velocities of  $V_1 = 2.5$  mm/min,  $V_2 = 25$  mm/min and  $V_3 = 250$  mm/min which were the same applied during the experiments. Moreover, a predefined room temperature of 298 °K was assigned to the whole specimen at the initial step for all cases. It should be mentioned that isothermal heat condition with constant temperature throughout the deformation was assumed for all loading rates except for the higher rate of  $V_3 = 250$  mm/min where 10% of the heat generated from the plastic work was assumed to stay inside the material throughout the deformation which adds up to the initial temperature.



**Figure 36: Mesh density of plain stress elements used in the FE simulation**

Figure 37 shows a sample deformation process for the specimen at  $V = 2.5$  mm/min. The deformed specimen clearly illustrates the necking failure mode encountered during the experimental tests. Additionally, the force-displacement results obtained from the FE modeling compare very well with their experimental counterparts for all loading rate considered as shown in Figure 38.

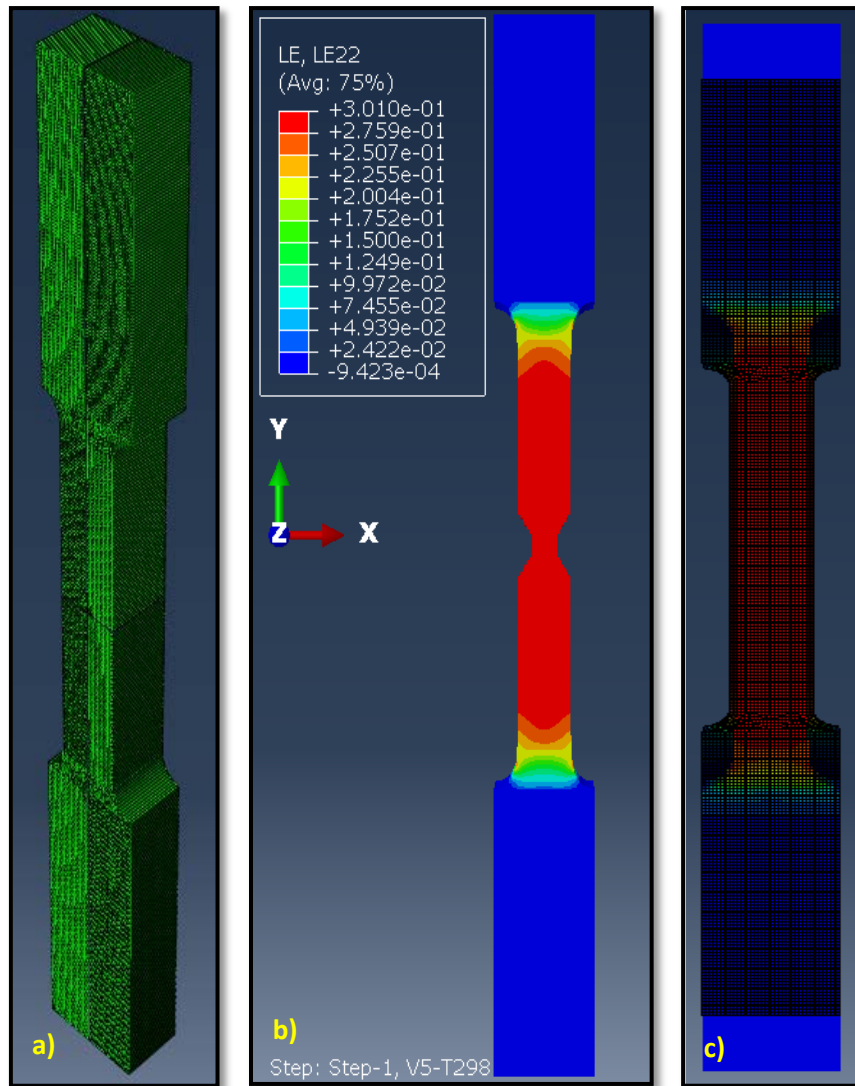


Figure 37: Sample deformation process for strain rate  $0.0015s^{-1}$  at room temperature, a) Un-deformed specimen, b) Deformed specimen, and c) Overlapping of deformed and un-deformed plot.

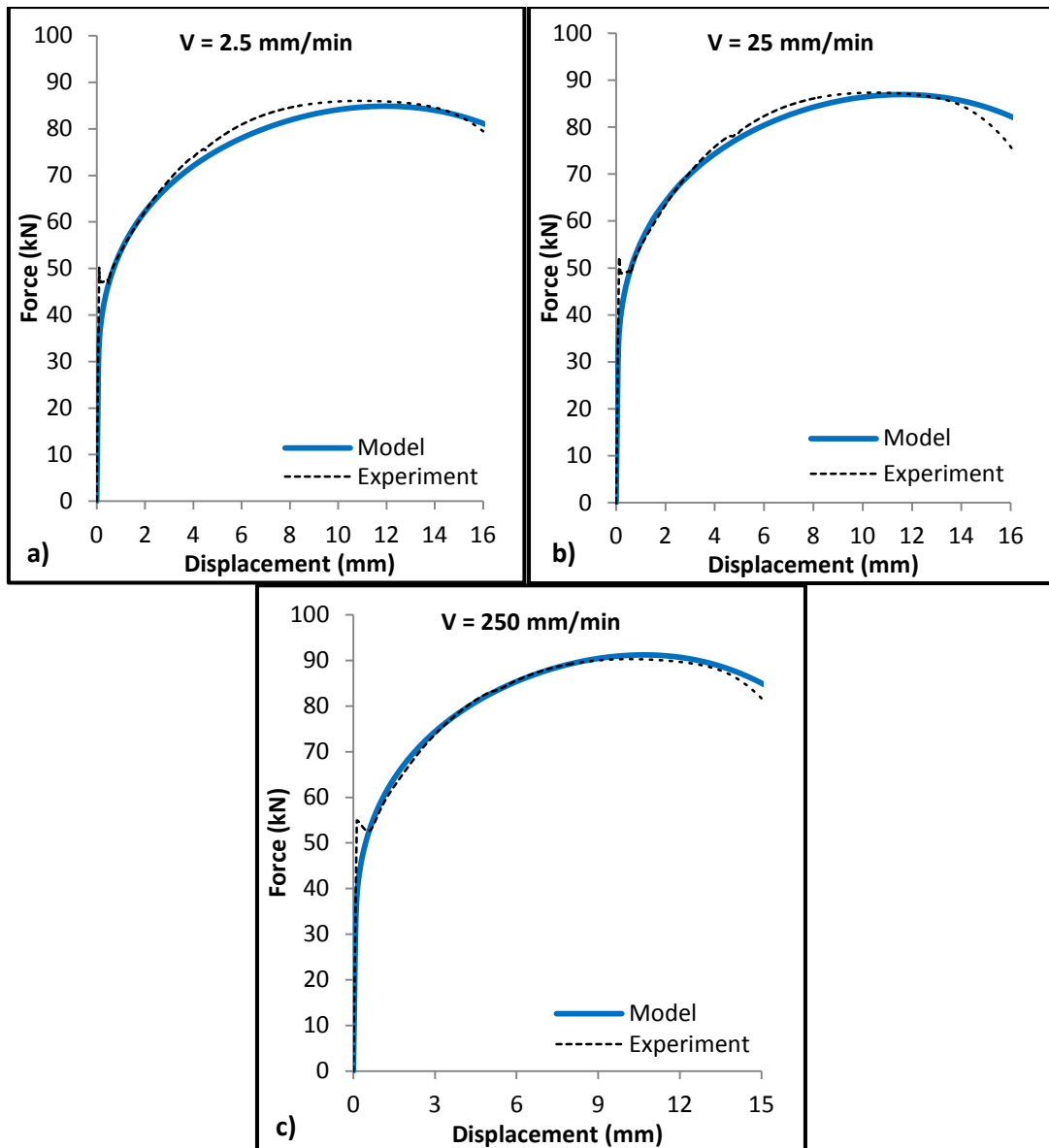


Figure 38: Force-Disp. curves at T = 298 °K for a) V = 2.5 mm/min, b) V = 25 mm/min, and c) V = 250 mm/min

### 5.3 Drop Hammer Test Simulation

The final step in the present finite element simulation is to simulate the drop hammer tests using the verified JC-damage model. The two drop hammer tests conducted during the experiments were simulated in this study using the same dimensions, hammer weights and drop heights as listed in Table 4. Because of its cylindrical shape, the specimen was modeled using axisymmetric finite element formulation at which only half of the specimen was simulated.

The FE modeling of the drop hammer test included three main parts; the hammer, the specimen, and the rigid ground (base). Each part was meshed using axisymmetric elements but with different mesh configurations as given in Table 8 and also displayed in Figures 39 through 41. The specimen was uniformly meshed with overall element size of 0.0004 as shown in Figure 39. The hammer and the ground parts were meshed with two different mesh controls; the regions of the contact with the specimen were modeled using fine mesh configurations of 0.0004 whereas, a coarse mesh configuration was assigned to the regions away from the contact. The mesh configurations for the hammer and the rigid ground are illustrated in Figures 40 and 41, respectively. The ground was modeled as rigid cylindrical dense material with height of 0.5m and diameter of 0.3m.

**Table 8: Mesh size for drop hammer test simulation**

Location	Mesh Size		
	Hammer	Specimen	Ground
Contact Area	0.0004	0.0004	0.0004
Non-Contact Area	0.001	Not Applicable	0.001

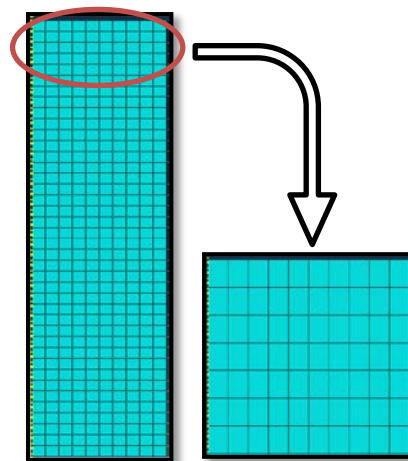


**Figure 39: Mesh configuration for the specimen used in the drop hammer test**

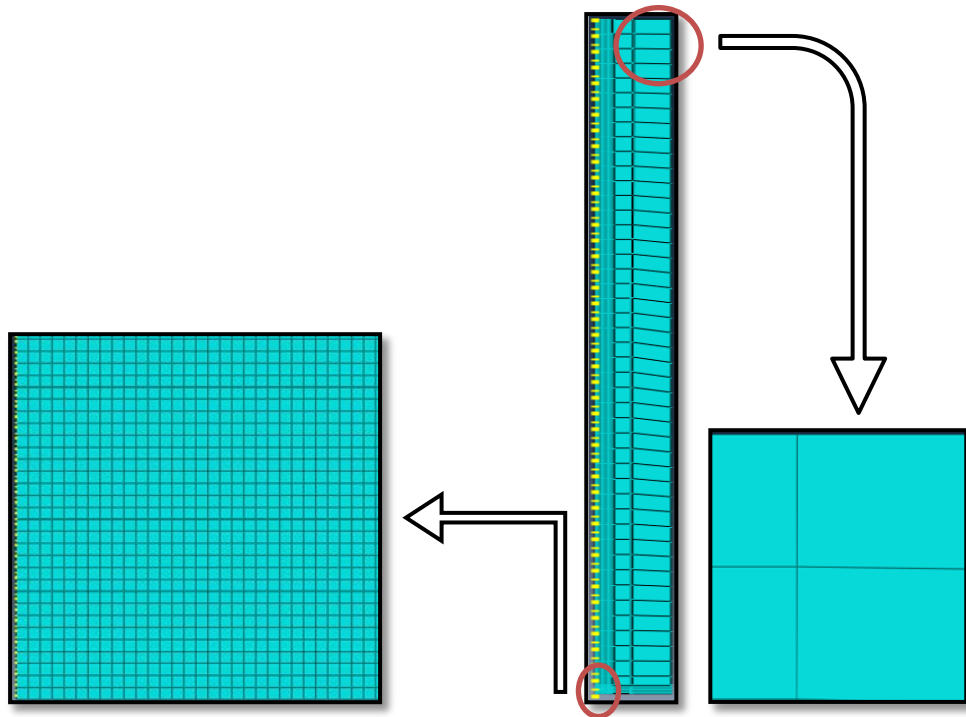


**Figure 40: Mesh configuration for hammer mass used in the drop hammer test**

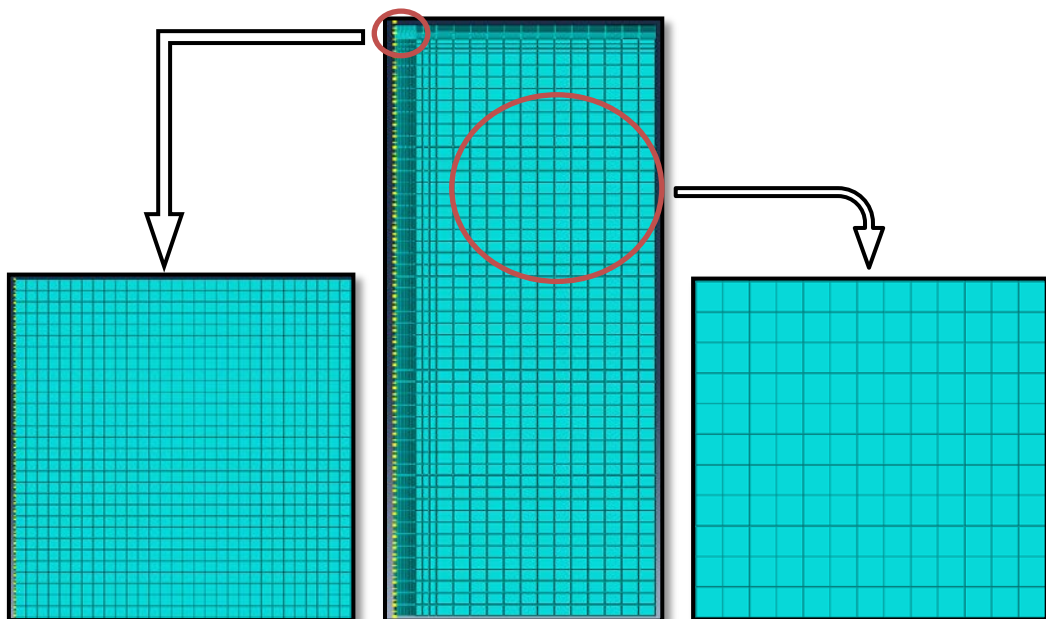


**Figure 41: Mesh configuration for the rigid base used in the drop hammer test**

To simulate the actual loading conditions encountered during the experiments, the free falling of the hammer was simulated by assigning a gravitational load with acceleration equal to  $9.81\text{m/s}$ . The contact between the surfaces was defined as a surface to surface contact with all self-contact interaction.

The ground was restricted from movement in all directions. Since these types of tests results in a moderate velocity impact and high strain rate of deformation, adiabatic deformation was considered in the analysis by assuming only 50% of the heat generated from the plastic work is dissipated outside. The simulation was then submitted and the deformation process was successfully captured for each loading scenario. Figure 42 shows an example of drop hammer deformation process at different time increments.

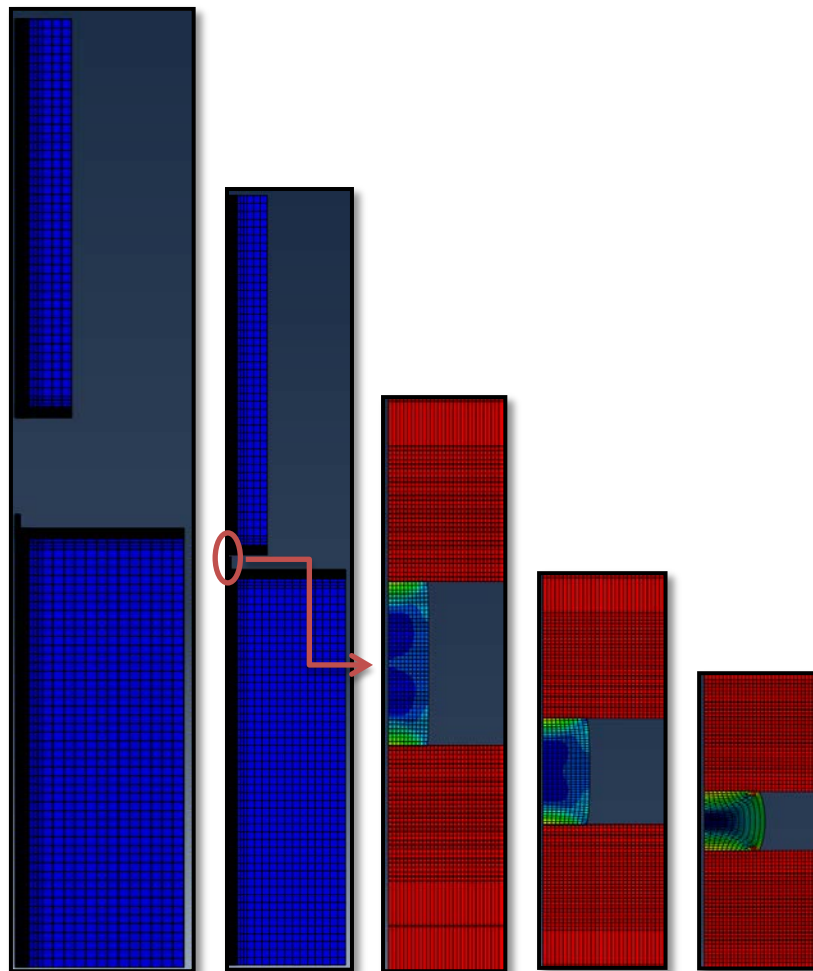


**Figure 42: Deformation process for strain rate  $550 \text{ s}^{-1}$**

The accuracy of the drop hammer FE simulation was also verified by comparisons with the experimental results in terms of the dimensions of the deformed specimens and the corresponding force-displacement results. The final dimensions of the sample compared to the experimental results are shown in Table 9. The comparison shows that the FE simulation was able to capture the deformed

configuration of the specimen. Also, Figure 43 shows a sample comparison between the test deformed shape and the FE simulation deformed shape.

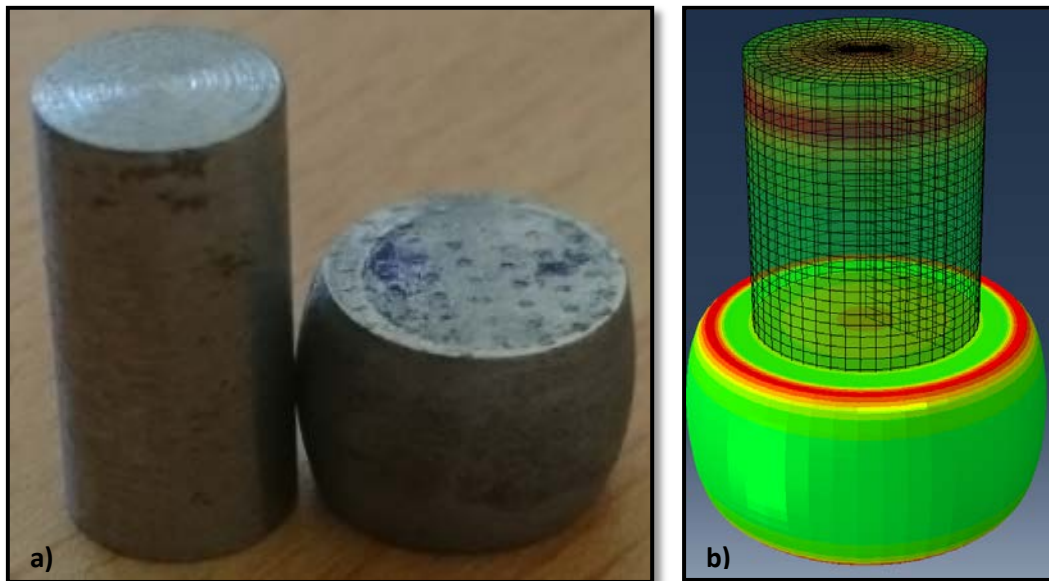


**Figure 43: Comparison between the experiment deformed specimen and the FE simulation deformed specimen, a) Experiment deformed specimen and b) FE simulation deformed specimen overlapping with the un-deformed specimen**

**Table 9: Final Dimensions of Specimens, Experiment and Model**

Strain Rate ( $s^{-1}$ )	390		550	
	Experiment	Model	Experiment	Model
Final Height (mm)	8.33	6.317	6.86	6.36
Final Diameter (mm)	11.1	13.0136	12.75	12.98518

The FE simulation results for the force-displacement relationship were also compared with the experiments for both loading scenarios as presented in Figure 44. The FE model, as can be seen from the figure, successfully captured the trend of force versus deformation with slight deviation from the experimental values. This deviation could be attributed to the fact that, during the experiment, the hammer was rebounding causing this variation in the forces.

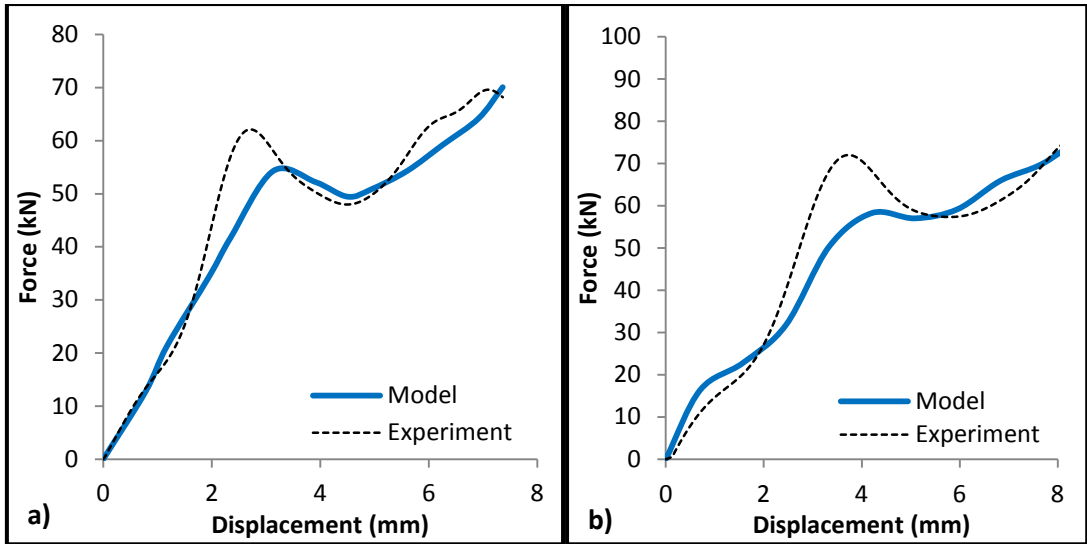


**Figure 44: Contact forces-displacement curves for strain rates a)  $390\text{s}^{-1}$  and b)  $550\text{s}^{-1}$**

The good comparisons presented in this chapter may surely be attributed to the accurate description of the material response through the coupled JC-damage model definition. Therefore, it is efficient to conclude that the present JC model can be extended to simulate different structural problems with different loading scenarios but within the room temperature.

## Chapter 6 : Conclusion and Remarks

### 6.1 Summary and Conclusions

The C45 steel is increasingly being used as structural material in the oil and gas industry. The material response to typical loading conditions experienced in such environment needs to be tested and evaluated. Hence, a comprehensive assessment of the thermo-mechanical response of this type of high strength steel is timely and necessary for design purposes.

This research studied the thermo-mechanical behavior of C45 structural steel based on the results of a series of experimental tests that were conducted by other researchers at different levels of temperatures (298 °K – 923 °K) at strain rates up to  $550\text{s}^{-1}$ . The corresponding true stress-true strain results were utilized to identify the material constants for the Johnson-Cook (JC) constitutive equation which was required to understand quantitatively the deformation behavior of this material. Scanning electron microscopy (SEM) was utilized to understand the microstructure of the material and measure the internal micro-cracks and voids for C45 steel at fracture for each test condition. The SEM results were then implemented in an energy-based damage model to define the evolution of damage throughout the deformation process. The damage model was integrated into the JC plasticity model to accurately describe the flow stress of C45 steel. The coupled JC-damage model was then implemented into the finite element software ABAQUS to simulate the experimental tests. The FE model developed in this analysis was verified using the experimental results conducted prior to this research work. The main objective of the numerical analysis was to develop a robust FE model that could be extended to simulate other structural problems that involve the use of C45 structural steel subjected to different loadings.

Based on the approach followed above, the following conclusions can be drawn:

- The quasi-static tests results at high temperatures revealed the typical degradation trend of the thermal stresses with temperature increase. However, dynamic strain aging (DSA) took place at certain combination of temperatures and strain rates which increase with the strain. The DSA is usually

characterized by the sudden jump in the thermal stress variation with temperature. This DSA phenomenon was clearly observed at 523 °K for the case of  $0.0015\text{s}^{-1}$  strain rate and at 723 °K for the higher rate.

- The yield stress increased with the increase of strain rate and decreased with temperature except in the regions where the DSA is active. On the other hand, the strain hardening was found to be almost rate-independent at room temperature. However, the rate dependency behavior of the material increased with temperature.
- A constitutive description of C45 steel is required to simulate the flow stress of the material. Thus, the experimental results and observations should be included and addressed properly in order to have a suitable flow stress model for this material. In this research, the empirical relation of JC constitutive model was selected to describe the material response. The DSA effects; however, were not captured in the present model.
- The JC model parameters extracted from the experimental results showed promising results at room temperature and fair matching at higher temperatures except for the regions where DSA is occurring.
- The energy-based damage model successfully captured the damage evolution within the microstructure of the material and the failure mode beyond the ultimate point. Therefore, the model is recommended to be used for different metals and at different loading regimes.

## **6.2 Limitations and Future Research**

The application of this research outcomes is limited to the loading conditions considered in the present experimental program to get accurate results. Any other scenarios intended to be implemented shall consider further experimental tests and exploration. Also, the DSA phenomenon should be studied further in order to understand its effect on the material response. To capture such effect, a physical-based constitutive model should be developed to accurately describe the plasticity behavior of C45 steel. The model should be able not only to address the plastic deformation that is attributed to the motion of dislocations but also to include the plastic flow in the range of temperatures and strain rates where diffusion and creep are dominant, i.e., the regions where DSA is active.

## References

1. T. Moan, '*Safety of Offshore Structures*', Centre for Offshore Research & Engineering (CORE), Singapore, 2004.
2. N. Haritos, '*Introduction to the Analysis and Design of Offshore Structures – An Overview*', eJSE International, no., pp. 55-65, 2007.
3. R. Al-Himairee, '*Characterization and Modeling of Damage in Steel at Different Strain Rates*', Master of Science in Civil Engineering, American University of Sharjah, 2011.
4. F. Abed and F. Makarem, '*Comparisons of Constitutive Models for Steel Over a Wide Range of Temperatures and Strain Rates*', J. Eng. Mater. Technol., vol. 134, no. 2, p. 021001, 2012.
5. K. Hoge and A. Mukherjee, '*The temperature and strain rate dependence of the flow stress of tantalum*', Journal of Materials Science, vol. 12, no. 8, pp. 1666-1672, 1977.
6. S. Chen and G. Gray, '*Constitutive behavior of tantalum and tantalum-tungsten alloys*', Metallurgical and Materials Transactions A, vol. 27, no. 10, pp. 2994-3006, 1996.
7. D. Goto, R. Garrett, J. Bingert, S. Chen and G. Gray, '*The mechanical threshold stress constitutive-strength model description of HY-100 steel*', Metall and Mat Trans A, vol. 31, no. 8, pp. 1985-1996, 2000.
8. B. Banerjee, '*The Mechanical Threshold Stress model for various tempers of AISI 4340 steel*', International Journal of Solids and Structures, vol. 44, no. 3-4, pp. 834-859, 2007.
9. E. Puchi-Cabrera, C. Villalobos-Gutiérrez and G. Castro-Fariñas, '*On the Mechanical Threshold Stress of Aluminum: Effect of the Alloying Content*', J. Eng. Mater. Technol., vol. 123, no. 2, p. 155, 2001.
10. Abed, Farid H., Adil K. Al-Tamimi, and Reem M. Al-Himairee. '*Characterization and Modeling of Ductile Damage in Structural Steel at Low and Intermediate Strain Rates*'. Journal of Engineering Mechanics 138.9 (2012): 1186-1194.
11. B. Darras, F. Abed, A. Abdul-Latif and S. Pervaiz, "*Experimental Investigation of Deformation in 5083 Marine-Grade Aluminum Alloy at Elevated*

- Temperatures*”, J. of Materi Eng and Perform, vol. 24, no. 4, pp. 1663-1668, 2015.
12. C. Thompson, Alan. '*High Strain Rate Characterization Of Advanced High Strength Steels*'. Master of Applied Science in Mechanical Engineering. the University of Waterloo, 2006.
  13. Guo, Wei-Guo, and Sia Nemat-Nasser. '*Flow Stress Of Nitronic-50 Stainless Steel Over A Wide Range Of Strain Rates And Temperatures*'. *Mechanics of Materials* 38.11 (2006): 1090-1103.
  14. F. Abed and G. Voyiadjis, "*Adiabatic Shear Band Localizations in BCC Metals at High Strain Rates and Various Initial Temperatures*", *Int J Mult Comp Eng*, vol. 5, no. 3-4, pp. 325-349, 2007.
  15. Lee, Woei-Shyan et al. '*Dynamic Mechanical Response Of Biomedical 316L Stainless Steel As Function Of Strain Rate And Temperature*'. *Bioinorganic Chemistry and Applications* 2011 (2011): 1-13.
  16. Lee, Y et al. '*A Study For The Constitutive Equation Of Carbon Steel Subjected To Large Strains, High Temperatures And High Strain Rates*'. *Journal of Materials Processing Technology* 130-131 (2002): 181-188.
  17. Lim, Hojun et al. '*A Physically Based Model Of Temperature And Strain Rate Dependent Yield In BCC Metals: Implementation Into Crystal Plasticity*'. *Journal of the Mechanics and Physics of Solids* 74 (2015): 80-96.
  18. Nemat-Nasser, Sia, Wei-Guo Guo, and David P. Kihl. '*Thermomechanical Response Of AL-6XN Stainless Steel Over A Wide Range Of Strain Rates And Temperatures*'. *Journal of the Mechanics and Physics of Solids* 49.8 (2001): 1823-1846.
  19. Sakumoto, Y. et al. '*High Temperature Properties Of Fire Resistant Steel For Buildings*'. *Journal of Structural Engineering* 118.2 (1992): 392-407.
  20. Su, J. et al. '*Plastic Behavior And Constitutive Relations Of DH-36 Steel Over A Wide Spectrum Of Strain Rates And Temperatures Under Tension*'. *Mechanics of Materials* 65 (2013): 76-87.
  21. Sung, Ji Hyun, Ji Hoon Kim, and R.H. Wagoner. '*A Plastic Constitutive Equation Incorporating Strain, Strain-Rate, And Temperature*'. *International Journal of Plasticity* 26.12 (2010): 1746-1771.

22. Tao, Zhong, Xing-Qiang Wang, and Brian Uy. '*Stress-Strain Curves Of Structural And Reinforcing Steels After Exposure To Elevated Temperatures*'. J. Mater. Civ. Eng. 25.9 (2013): 1306-1316.
23. Vaynman, S. et al. '*Effect Of Strain Rate And Temperature On Mechanical Properties And Fracture Mode Of High Strength Precipitation Hardened Ferritic Steels*'. Scripta Materialia 55.4 (2006): 351-354.
24. Wang, Wei-yong, Bing Liu, and Venkatesh Kodur. '*Effect Of Temperature On Strength And Elastic Modulus Of High-Strength Steel*'. J. Mater. Civ. Eng. 25.2 (2013): 174-182.
25. F. Abed, F. Makarem and G. Voyiadjis, "*Dynamic Localizations in HSLA-65 and DH-36 Structural Steel at Elevated Temperatures*", J. Eng. Mater. Technol., vol. 135, no. 2, p. 021007, 2013.
26. S. Nemat-Nasser, W. Guo, "*Thermomechanical response of HSLA-65 steel plates: experimental and modeling*," Mechanics of Material, vol. 37, no. 5, pp. 379-405, May 2005.
27. S. Nemat-Nasser and W. Guo, "*Thermomechanical response of DH-36 structural steel over a wide range of strain rates and temperatures*," Mechanics of Materials, vol. 35, no. 11, pp. 1023-1047, 2003.
28. F. H. Abed and G. Voyiaddjis, "*Plastic deformation modeling of Al-6XN stainless steel at low and high strain rates and temperatures using a combination of bcc and fcc mechanism of metals*," Int. J. Plasticity, vol. 21, pp. 1618-1639, 2004.
29. E. Kishta, F. Abed and B. Darras, "*Nonlinear Finite Element Simulation of Friction Stir Processing of Marine Grade 5083 Aluminum Alloy*", Engineering Transactions, vol. 62, no. 4, pp. 313-328, 2014.
30. F. Makarem and F. Abed, "*Nonlinear finite element modeling of dynamic localizations in high strength steel columns under impact*", International Journal of Impact Engineering, vol. 52, pp. 47-61, 2013.
31. F. Abed, "*On the differences of dynamic localizations between different types of metals*", IJMSI, vol. 4, no. 234, p. 215, 2010.
32. G. Voyiadjis and F. Abed, "*Transient localizations in metals using microstructure-based yield surfaces*", Modelling and Simulation in Materials Science and Engineering, vol. 15, no. 1, pp. S83-S95, 2006.

33. B. Darras, F. Abed, S. Pervaiz and A. Abdu-Latif, "*Analysis of damage in 5083 aluminum alloy deformed at different strainrates*", *Materials Science and Engineering: A*, vol. 568, pp. 143-149, 2013.
34. Celentano, Diego J., and Jean-Louis Chaboche. '*Experimental And Numerical Characterization Of Damage Evolution In Steels*'. *International Journal of Plasticity* 23.10-11 (2007): 1739-1762.
35. Chae, D., and D.A. Koss. '*Damage Accumulation And Failure Of HSLA-100 Steel*'. *Materials Science and Engineering: A* 366.2 (2004): 299-309.
36. Abed, F, and G. Voyiadjis. '*Plastic Deformation Modeling Of AL-6XN Stainless Steel At Low And High Strain Rates And Temperatures Using A Combination Of Bcc And Fcc Mechanisms Of Metals*'. *International Journal of Plasticity* 21.8 (2005): 1618-1639.
37. Al-Himairee, Reem Majeed, Farid Hamid Abed, and Adil K. Al-Tamimi. '*Damage Evolution In Structural Steel At Different Loading Conditions*'. *KEM* 471-472 (2011): 969-974.
38. Chen, Ju, Ben Young, and Brian Uy. '*Behavior Of High Strength Structural Steel At Elevated Temperatures*'. *Journal of Structural Engineering* 132.12 (2006): 1948-1954.
39. Rohr, I. et al. '*Material Characterization And Constitutive Modelling Of A Tungsten-Sintered Alloy For A Wide Range Of Strain Rates*'. *International Journal of Impact Engineering* 35.8 (2008): 811-819.
40. Rohr, I., H. Nahme, and K. Thoma. '*Material Characterization And Constitutive Modelling Of Ductile High Strength Steel For A Wide Range Of Strain Rates*'. *International Journal of Impact Engineering* 31.4 (2005): 401-433.
41. G.R. Johnson, W.H. Cook, 'A constitutive model and data for metals subjected to large strains, high strain rates and high', *Proceedings of the 7th International Symposium on Ballistics*, 541-547, retrieved 2009.
42. D. Steinberg, S. Cochran and M. Guinan, '*A constitutive model for metals applicable at high-strain rate*', *J. Appl. Phys.*, vol. 51, no. 3, p. 1498, 1980.
43. D. Steinberg and C. Lund, '*A constitutive model for strain rates from  $10^{-4}$  to  $10^6$   $s^{-1}$* ', *J. Appl. Phys.*, vol. 65, no. 4, p. 1528, 1989.
44. F. Zerilli and R. Armstrong, '*Dislocation-mechanics-based constitutive relations for material dynamics calculations*', *J. Appl. Phys.*, vol. 61, no. 5, p. 1816, 1987.

45. F. Abed, T. Jankowiak and A. Rusinek, "*Verification of a Thermoviscoplastic Constitutive Relation for Brass Material Using Taylor's Test*", J. Eng. Mater. Technol, vol. 137, no. 4, p. 041005, 2015.
46. F. Abed and G. Voyiadjis, "*Thermodynamic Consistent Formulations of Viscoplastic Deformations in FCC Metals*", J. Eng. Mech., vol. 133, no. 1, pp. 76-86, 2007.
47. Triton Alloys Inc ., "C45 steel plate suppliers -Triton Alloys Inc", 2016. [Online]. Available: <http://www.tritonalloysinc.com/en-10025-2-steel/steel-plate-bs-en-10025-2-steel-grade-plate/steel-plate-type-c-45-plate/#what>. [Accessed: 10- Mar- 2015].
48. Triton Alloys Inc ., "offshore steel suppliers | offshore structural steel plate", 2016. [Online]. Available: <http://www.tritonalloysinc.com/offshore-structural-steel/offshore-structural-plate-steel-plate/steel-plate-type-offshore-structural-steel-plate/#specification>. [Accessed: 10- Mar- 2015]
49. Chen, Haifeng, Jinyuan Tang, and Wei Zhou. '*An Experimental Study Of The Effects Of Ultrasonic Vibration On Grinding Surface Roughness Of C45 Carbon Steel*'. Int J Adv Manuf Technol 68.9-12 (2013): 2095-2098.
50. Glowacki, Mirosław, and Marcin Hojny. 'Computer-Aided Investigation Of Mechanical Properties For Integrated Casting And Rolling Processes Using Hybrid Numerical-Analytical Model Of Mushy Steel Deformation'. The Sixth International Conference On Advanced Engineering Computing And Applications In Sciences. Kraków, Poland: IARIA, 2012. 83-89.
51. 'Influence of Different Material Models on the Result of Numerical High Speed Cutting Simulations'. 1<sup>st</sup> International Conference On High Speed Forming. Germany: N.p., 2004. 133-142.
52. 'Influence of Heating Rate on Sorbitic Transformation Temperature of Tempering C45 Steel'. Archives of Foundry Engineering 11.Special Issue 2/2011 (2011): 131-134.
53. "Investigation Of The Strain-Hardening Behavior Of Modern Lightweight Steels Considering The Forming Temperature And Forming Rate." Luxembourg: European Commission, Research Fund for Coal and Steel, 2008. Contact: RFCS Publications.

54. Kermouche, G, and C Langlade. 'Mechanical Nano-Structuration Of A C45 Steel Under Repeated Normal Impacts'. IOP Conference Series: Materials Science and Engineering 63 (2014): 012019.
55. Król, S. et al. '*Friction And Wear Properties Of Titanium And Oxidised Titanium In Dry Sliding Against Hardened C45 Steel*'. Journal of Materials Processing Technology 157-158 (2004): 364-369.
56. Leppert, Tadeusz. '*Effect Of Cooling And Lubrication Conditions On Surface Topography And Turning Process Of C45 Steel*'. International Journal of Machine Tools and Manufacture 51.2 (2011): 120-126.
57. Magnabosco, I. et al. '*Induction Heat Treatment Of A ISO C45 Steel Bar: Experimental And Numerical Analysis*'. Computational Materials Science 35.2 (2006): 98-106.
58. Michalik, Peter et al. '*Monitoring Surface Roughness Of Thin-Walled Components From Steel C45 Machining Down And Up Milling*'. Measurement 58 (2014): 416-428.
59. "Minimizing The Distortion Of Steel Profiles By Controlled Cooling." Otto-von-Guericke-University, Magdeburg / Germany: Steel Institute VDEh, Max-Planck-Institut für Eisenforschung, and Austrian Society for Metallurgy and Materials ASMET, 2005. Materials Technology - Carbon Steels.
60. '*Numerical Modelling Of Steel Deformation At Extra-High Temperatures*'. Numerical Modelling. 1<sup>st</sup> ed. InTech, 2012. 255-276. 6 May 2015.
61. Rajanna, K., B. Pathiraj, and B.H. Kolster. '*Some Studies On The Influence Of Stress Ratio And Test Temperature On X-Ray Fractography Observations In C45 Steel Specimens*'. Engineering Fracture Mechanics 54.4 (1996): 457-470.
62. Savran, V.I. et al. '*Microstructural Features Of Austenite Formation In C35 And C45 Alloys*'. Metal and Mat Trans A 38.5 (2007): 946-955.
63. SreeramaReddy, T.V. et al. '*Machinability Of C45 Steel With Deep Cryogenic Treated Tungsten Carbide Cutting Tool Inserts*'. International Journal of Refractory Metals and Hard Materials 27.1 (2009): 181-185.
64. Szkodo, M. '*Relationship Between Microstructure Of Laser Alloyed C45 Steel And Its Cavitation Resistance*'. Journal of Materials Processing Technology 162-163 (2005): 410-415.

65. Wang, L., K.S. Nam, and S.C. Kwon. '*Effect Of Plasma Nitriding Of Electroplated Chromium Coatings On The Corrosion Protection C45 Mild Steel*'. Surface and Coatings Technology 202.2 (2007): 203-207.
66. Yan, P.X et al. '*Post Boronizing Ion Implantation Of C45 Steel*'. Applied Surface Science 195.1-4 (2002): 74-79.
67. S. Nemat-Nasser, W. Guo, "*Thermomechanical response of HSLA-65 steel plates: experimental and modeling,*" Mechanics of Material, vol. 37, no. 5, pp. 379-405, May 2005.
68. S. Nemat-Nasser and W. Guo, "*Thermomechanical response of DH-36 structural steel over a wide range of strain rates and temperatures,*" Mechanics of Materials, vol. 35, no. 11, pp. 1023-1047, 2003.
69. F. H. Abed and G. Voyiadjis, "*Plastic deformation modeling of Al-6XN stainless steel at low and high strain rates and temperatures using a combination of bcc and fcc mechanism of metals,*" Int. J. Plasticity, vol. 21, pp. 1618-1639, 2004.
70. P. Follansbee and U. Kocks, '*A constitutive description of the deformation of copper based on the use of the mechanical threshold stress as an internal state variable*', Acta Metallurgica, vol. 36, no. 1, pp. 81-93, 1988.
71. U. Kocks, '*Realistic constitutive relations for metal plasticity*', Materials Science and Engineering: A, vol. 317, no. 1-2, pp. 181-187, 2001.
72. Farid H. Abed, "*Constitutive modeling of the mechanical behavior of high strength ferritic steel for static and dynamic applications,*" Mechanics of Time-Dependent Materials Journal, vol. 14, pp. 329-345, 2010.
73. F. Abed, S. Ranganathan and M. Serry, '*Constitutive modeling of nitrogen-alloyed austenitic stainless steel at low and high strain rates and temperatures*', Mechanics of Materials, vol. 77, pp. 142-157, 2014.
74. S. Hirdaris, W. Bai, D. Dessi, A. Ergin, X. Gu, O. Hermundstad, R. Huijsmans, K. Iijima, U. Nielsen, J. Parunov, N. Fonseca, A. Papanikolaou, K. Argyriadis and A. Incecik, '*Loads for use in the design of ships and offshore structures*', Ocean Engineering, vol. 78, pp. 131-174, 2014.
75. G. Voyiadjis, "*Handbook of damage mechanics.*" New York: Springer, 2015.
76. D. Krajcinovic, "*Damage mechanics.*" Amsterdam: Elsevier, 1996.
77. S. Murakami, "*Continuum damage mechanics.*" Dordrecht: Springer, 2012.

78. G. Voyiadjis and P. Kattan, "*Damage mechanics.*" Boca Raton: Taylor & Francis, 2005.
79. L. Kachanov, "*Introduction to continuum damage mechanics.*" Dordrecht: M. Nijhoff, 1986.
80. Directindustry.com, "Electromechanical universal testing machine - WDW series - Laryee Technology Co., Ltd.", 2016. [Online]. Available: <http://www.directindustry.com/prod/laryee-technology-co-ltd/product-66945-481801.html>. [Accessed: 07- Apr- 2015].
81. Directindustry.com, "Laboratory Equipment, Climate test chambers - All industrial manufacturers in this category - Videos - Page 4", 2016. [Online]. Available: [http://www.directindustry.com/cat/laboratory-equipment/climate-test-chambers-BQ-534-\\_4.html](http://www.directindustry.com/cat/laboratory-equipment/climate-test-chambers-BQ-534-_4.html). [Accessed: 07- Apr- 2015].
82. Reichel-partner.com, "BAM Fallhammer |", 2016. [Online]. Available: <http://reichel-partner.com/index.php/bam-fallhammer/>. [Accessed: 10- Apr- 2015].
83. Thelibraryofmanufacturing.com, "Drop Forging Hammers", 2016. [Online]. Available: [http://thelibraryofmanufacturing.com/forging\\_hammers.html](http://thelibraryofmanufacturing.com/forging_hammers.html). [Accessed: 10- Apr- 2015].
84. Wikipedia, "Scanning electron microscope", 2016. [Online]. Available: [https://en.wikipedia.org/wiki/Scanning\\_electron\\_microscope](https://en.wikipedia.org/wiki/Scanning_electron_microscope). [Accessed: 15- May- 2015].
85. W. Wang, B. Liu and V. Kodur, "*Effect of Temperature on Strength and Elastic Modulus of High-Strength Steel*", J. Mater. Civ. Eng., vol. 25, no. 2, pp. 174-182, 2013.
86. European Convention for Constructional Steelworks (ECCS). (2001). "Material properties." European recommendations for the fire safety of steel structures, Section III.2, ECCS General Secretariat, Brussels, Belgium.
87. AISC. (2005). "Specification for structural steel buildings." ANSI/AISC 2005:360-05, Chicago.
88. British Standards Institution (BSI). (1990). "The structural use of steelwork in buildings, Part 8: Code of practice for fire resistant design." BS5950, London.
89. European Committee for Standardization (CEN). (2005b). "Eurocode 3: Design of steel structures—Part 1.2: General rules for structural fire design." BS EN1993-1-2, Brussels, Belgium.

90. European Committee for Standardization (CEN). (2006). "Eurocode 4: Design of composite steel and concrete structures: Part 1.1: General rules and rules for buildings." BS EN1994-1-1, Brussels, Belgium.
91. T. Wang, J. Jonas, H. Qin and S. Yue, "*Effect of dynamic strain aging on the deformation and twinning behavior of a Mg–2Zn–2Nd alloy*", Materials Science and Engineering: A, vol. 645, pp. 126-135, 2015.
92. Rasband, W.S., ImageJ, U. S. National Institutes of Health, Bethesda, Maryland, USA, <http://imagej.nih.gov/ij/>, 1997-2015.
93. G. Voyiadjis and F. Abed, "*Effect of dislocation density evolution on the thermomechanical response of metals with different crystal structures at low and high strain rates and temperatures*", Archives of Mechanics, vol. 57, no. 4, pp. 299 - 343, 2005.
94. Abaqus 6.14. SIMULIA, Dassault Systèmes.

## **Vita**

Mohammad Hassan Saffarini was born on September 27<sup>th</sup>, 1990, in Al Zarqa'a City, Hashemite Kingdom of Jordan. He studied in Sharjah during high school and was honored to be ranked the fifteenth in class over UAE and the fifth over Sharjah in 2008. He was awarded Ministry of Presidential Affairs (MOPA) Scholarship to study Civil Engineering in the American University of Sharjah and received his Bachelor degree in Fall 2012. Mohammad started his master degree at the American University of Sharjah in spring 2013 and was working as an offshore methods engineer for a respected contractor in the oil and gas industry called Saipem Contracting Netherlands B.V.